DOI: 10.1113/JP277724

A computational model of induced pluripotent stem-cell derived cardiomyocytes incorporating experimental variability from multiple data sources

Divya C. Kernik[1], Stefano Morotti[2], HaoDi Wu[3], Priyanka Garg[3], Henry J. Duff[7], Junko Kurokawa[6], José Jalife[4,5], Joseph C. Wu[3], Eleonora Grandi*[2] and Colleen E. Clancy*[1]

*Corresponding Authors

[1]Colleen E. Clancy, Ph.D. - email: ceclancy@ucdavis.edu
Department of Physiology and Membrane Biology
Department of Pharmacology

School of Medicine

University of California, Davis
Tupper Hall, RM 4303
Davis, CA 95616-8636

[2]Eleonora Grandi, Ph.D. - email: egrandi@ucdavis.edu
Department of Pharmacology

School of Medicine

University of California, Davis
Tupper Hall, RM 2427
Davis, CA 95616-8636

[3]Joseph C. Wu, MD, Ph.D. - email: joewu@stanford.edu

Director, Stanford Cardiovascular Institute

Department of Medicine

Division of Cardiovascular Medicine

Stanford University School of Medicine

Stanford, CA 94305

[4]Jose Jalife, MD – email: jjalife@umich.edu

Department of Internal Medicine

Center for Arrhythmia Research

Cardiovascular Research Center

University of Michigan

Ann Arbor, MI 48109

[5]Centro Nacional de Investigaciones Cardiovasculares (CNIC), and CIBERV

Madrid, Spain

[6]Junko Kurokawa, Ph.D. – email: junkokuro@u-shizuoka-ken.ac.jp

Department of Bio-Informational Pharmacology

School of Pharmaceutical Sciences

University of Shizuoka

Shizuoka, Japan

[7]Henry J. Duff, MD – email: hduff@ucalgary.ca

Libin Cardiovascular Institute of Alberta

Faculty of Medicine

University of Calgary

Calgary, AB, Canada

Running Title: Computational model of experimental variability in iPSC-CMs

Key Points:

- Induced pluripotent stem cell-derived cardiomyocytes (iPSC-CMs) capture patient-specific genotype-phenotype relationships, as well as cell-to-cell variability of cardiac electrical activity
- Computational modeling and simulation provide a high throughput approach to reconcile multiple datasets describing physiological variability, and identify vulnerable parameter regimes
- We have developed a whole-cell model of iPSC-CMs composed of single exponential voltage-dependent gating variable rate constants, parameterized to fit experimental iPSC-CM outputs
- We have utilized experimental data across multiple laboratories to model experimental variability and investigate subcellular phenotypic mechanisms in iPSC-CMs
- This framework links molecular mechanisms to cellular-level outputs by revealing unique subsets of model parameters linked to known iPSC-CM phenotypes

ABSTRACT:

There is a profound need to develop a strategy to predict patient-to-patient vulnerability in the emergence of cardiac arrhythmia. A promising *in vitro* method to address patient-specific proclivity to cardiac disease utilizes induced pluripotent stem cell-derived cardiomyocytes (iPSC-CMs). A major strength of this approach is that iPSC-CMs contain donor genetic information and therefore capture patient-specific genotype-phenotype relationships. A cited detriment of iPSC-CMs is the cell-to-cell variability observed in electrical activity. We postulated, however, that cell-to-cell variability may constitute a strength when appropriately

utilized in a computational framework to build cell populations that can be employed to identify phenotypic mechanisms and pinpoint key sensitive parameters. Thus, we have exploited variation in experimental data across multiple laboratories to develop a computational framework to investigate subcellular phenotypic mechanisms. We have developed a whole-cell model of iPSC-CMs composed of simple model components comprising ion channel models with single exponential voltage-dependent gating variable rate constants, parameterized to fit experimental iPSC-CM data for all major ionic currents. By optimizing ionic current model parameters to multiple experimental datasets, we incorporate experimentally-observed variability in the ionic currents. The resulting population of cellular models predicts robust inter-subject variability in iPSC-CMs. This approach links molecular mechanisms to known cellular-level iPSC-CM phenotypes, as we show by comparing immature and mature subpopulations of models to analyze contributing factors underlying each phenotype. In the future, the models presented can be readily expanded to include genetic mutations and pharmacological interventions to study the mechanisms of rare events, such as arrhythmia triggers.

INTRODUCTION:

Patient variability is one of the most daunting aspects of forecasting arrhythmia vulnerability in response to inherited disease or drug application. Considerable differences in drug impacts are routinely observed from patient to patient, with significant overlap between normal and pathological variants (Leopold & Loscalzo, 2018). However, genotype, and even sex, have not been sufficiently considered as a biological variable when developing pharmacotherapy regimes (Schwartz *et al.*, 1995; Schwartz *et al.*, 2001; Shah & Carter, 2008; Jamshidi *et al.*, 2012; Kaab *et al.*, 2012; Behr & Roden, 2013). There is a profound need to develop a strategy to predict the diverse mechanisms of arrhythmia vulnerability across patient populations.

A promising emerging experimental method utilizes induced pluripotent stem cell-derived cardiomyocytes (iPSC-CMs). iPSC-CMs are an increasingly utilized patient-specific cardiac cell model because they recapitulate cellular electrical properties of normal and diseased phenotypes, preserve patient-specific genotype, and demonstrate expected pharmacological responses of adult cardiomyocytes (Moretti *et al.*, 2010; Itzhaki *et al.*, 2011; Terrenoire *et al.*, 2013; Sallam *et al.*, 2015). iPSC-CMs derive from adult somatic cells reprogrammed to the embryonic-like state and then differentiated to cardiomyocytes (Takahashi & Yamanaka, 2006). Cell-based models for multiple cardiac diseases have been developed using iPSC-CMs and show preservation of patient-specific disease markers carried from the source

patient to the patient-derived iPSC-CMs (Moretti *et al.*, 2010; Itzhaki *et al.*, 2011; Lan *et al.*, 2013; Garg *et al.*, 2018). The retention of patient-specific disease markers makes iPSC-CMs an ideal tool for investigating patient-specific disease and response. Indeed, iPSC-CMs are currently being utilized in preclinical drug testing and prediction of genotype-phenotype relationships (Sun *et al.*, 2012; Lan *et al.*, 2013; Liang *et al.*, 2013; Navarrete *et al.*, 2013; Burridge *et al.*, 2016).

One of the limitations of iPSC-CMs as a model of adult cardiac behavior is their immature phenotype, which more closely resembles fetal cardiomyocytes. The immature iPSC-CM phenotype is characterized by spontaneous beating, significant differences in potassium currents compared to adult cardiac cells, and the presence of early-developmental currents (Bett *et al.*, 2013; Karakikes *et al.*, 2014). Additionally, iPSC-CMs have immature calcium handling due to their lack of T-tubules and differences in sarcoplasmic reticulum (SR) calcium handling (Yang *et al.*, 2014). Recent experimental developments have enhanced the maturation of iPSC-CMs by mimicking the natural environment which allows for staged transitions of cardiomyocytes from the embryonic to adult phenotype (Kamakura *et al.*, 2013; Nunes *et al.*, 2013; Herron *et al.*, 2016; Tiburcy *et al.*, 2017).

Another persistent concern with iPSC-CM technology has been the vast diversity of phenotypes observed *in vitro*. One reason for the variability between iPSC-CMs undoubtedly arises from the differences in genetic information of donors (DeBoever *et al.*, 2017). Variation due to genetic differences is a critical attribute of iPSC-CMs, as it allows for the observation of a variety of naturally occurring phenotypes and reflects patient-specific vulnerability to rare events, such as arrhythmia. However, even iPSC-CMs derived from the same donor with identical genetic information may display persistently variable phenotypes due to unknown sources of variation. There are a number of potential sources of variability, not least of all the complex process of generating and culturing iPSC-CMs and the influence of precise maturation phases (Narsinh *et al.*, 2011). Action potential (AP) morphologies and calcium transients (CaTs) have been shown to vary both within independent laboratories (Doss *et al.*, 2012; Du *et al.*, 2015), and across laboratories (Hwang *et al.*, 2015).

While the iPSC-CMs that are utilized *in vitro* allow for observation of a variety of responses to drugs and other perturbations, a major drawback in the experimental setting is the lack of a high throughput method to link underlying genomic, proteomic, or ionic mechanisms to the observed whole-cell behaviors. Population-based computational modeling provides a powerful tool in closing this gap through *in silico* analysis of variability in cardiac

electrophysiology (Muszkiewicz *et al.*, 2016; Yang *et al.*, 2016; Passini *et al.*, 2017; Ni *et al.*, 2018). Implementation of these approaches in the modeling and simulation of iPSC-CMs has the potential to reconcile multiple datasets, define physiological ranges of variability, and identify vulnerable parameter regimes (Sarkar & Sobie, 2010; Yang & Clancy, 2012; Britton *et al.*, 2013; Yang *et al.*, 2015; Morotti & Grandi, 2017). In using iPSC-CMs for cardiotoxicity testing of pharmacological interventions, the U.S. Food and Drug Administration (FDA) has outlined the Comprehensive In Vitro Proarrhythmia Assay (CiPA) protocol to combine cellular iPSC-CM outputs with computational approaches (Fermini *et al.*, 2015). These efforts will be further strengthened by a high throughput computational approach to study the mechanisms underlying phenotypic variability in iPSC-CMs.

While prior studies have addressed computational modeling of iPSC-CMs (Paci *et al.*, 2013; Koivumaki *et al.*, 2018), there is a need for a computational model which incorporates the wide-range of experimental measurements from iPSC-CMs. Paci et al. have developed a computational model of the iPSC-CM which is based on a single iPSC-CM experimental electrophysiology study. Due to the lack of experimental data available at the time, the model is largely based on I-V curves measured in iPSC-CMs by Ma et al. (2011). Model kinetics were largely retained from the ten Tusscher et al. adult ventricular model, with any additional changes based on experimental data from animal or adult human cells (ten Tusscher *et al.*, 2004; Paci *et al.*, 2012). Although this model captures the spontaneously beating iPSC-CM action potential phenotype, it is based on a limited description of iPSC-CM behavior. Later iterations of iPSC-CM models by Paci et al. (2018) and Koivumaki et al. (2018) incorporated modifications to improve calcium handling, however these adaptations were made with limited experimental data to define the range of calcium transient behavior during the AP. The model presented in this study is constrained by several calcium handling datasets which have not been utilized in parameterizing prior models, including concentration measurements of the iPSC-CM calcium transient during the AP.

Other computational studies have adapted the Paci et al. framework to model specific phenotypes and populations of iPSC-CMs (Lei *et al.*, 2017; Paci *et al.*, 2017; Koivumaki *et al.*, 2018; Paci *et al.*, 2018; Tveito *et al.*, 2018), however none of these efforts have utilized *in vitro* kinetics data to implement experimentally informed variation of iPSC-CMs. There is a wide range iPSC-CM phenotypes which are not captured by previous approaches to modeling iPSC-CMs. As there is a wide range of “normal” iPSC-CM behaviors characterized by distinct experimental laboratories, we present a comprehensive computational model that captures this experimental variability.

The goal of our study is to extend the iPSC-CM technology by developing an *in silico* complement: a high throughput method for analyzing phenotypic mechanisms of emergent behaviors in normal control iPSC-CMs. This is achieved by computationally modeling phenotypic variability in control iPSC-CMs through simple models based on source data from multiple labs. The use of simplified models to describe ionic gating kinetics allows us to fully parameterize a model to fit multiple individual experimental datasets. This approach allowed for rapid construction of model populations from multiple data sets, while setting the stage for future expansion into patient specific electrophysiology models by allowing reparameterization from data collected from donor cells.

Additionally, this allows us to ask if kinetic variability can explain whole-cell variation observed in iPSC-CMs experimentally. Here we show that predicted experimental variability at the subcellular level can recapitulate the full range of *in vitro* whole-cell iPSC-CM behavior in an *in silico* cellular population. The population can further be used to identify subpopulations of interest, including immature and mature phenotypes, and elucidate underlying processes that characterize the phenotypes. In the future, our approach can also be used to examine mechanism of disease and drug effects. The computational models of iPSC-CMs will allow for identification of parameter regimes with increased proclivity to arrhythmia in the presence of genetic mutation or pharmacological intervention. The tools may be applied for *in silico* screening and prediction of drug effects on varied genetic backgrounds to predict patient pharmacological responses**.**

METHODS:

All source code and instructions are freely available on the GitHub:
https://github.com/ClancyLabUCD/IPSC-model

Model Construction

As in prior cardiomyocytes models (Rudy & Silva, 2006), the iPSC-CM can be described by the differential equation:

$$\frac{dV}{dt} = \frac{-I_{ion} + I_{stim}}{C_m} \quad (1)$$

Where V is voltage, t is time, C_m is membrane capacitance, I_{ion} is the sum of transmembrane currents, and I_{stim} is the stimulus current (I_{stim} = 0 in spontaneously beating cells). The iPSC-

CM model (schematic representation in Fig. 1, left) includes 13 transmembrane currents, such that:

$$I_{ion} = I_{Na} + I_{CaL} + I_{Kr} + I_{Ks} + I_{K1} + I_{to} + I_f + I_{CaT} + I_{NCX} + I_{PMCA} + I_{NaK} + I_{bCa} + I_{bNa} \quad (2)$$

A schematic of the model cell containing all the ionic processes and compartments in the model is shown in Fig. 1. Seven key transmembrane currents (I_{Na}, I_{CaL}, I_{Kr}, I_{Ks}, I_{K1}, I_{to}, and I_f, indicated by red stars in Fig. 1), were reformulated using Hodgkin-Huxley-type gating formulations (Hodgkin & Huxley, 1952). For each of these currents, single exponential rate-constants (right panel, Fig. 1) were optimized to iPSC-CM experimental data (Fig. 2, step 1a). The remaining currents shown in Fig. 1 were modeled using formulations from previously published cardiac models (Shannon *et al.*, 2004; ten Tusscher *et al.*, 2004; Maltsev & Lakatta, 2009), and tuned to recapitulate experimental data for whole-cell outputs of iPSC-CMs. Details describing the experimental data used and resulting model formulations are in the results.

The iPSC-CM ion dynamics were formulated as has been done previously (DiFrancesco & Noble, 1985; Luo & Rudy, 1994; ten Tusscher *et al.*, 2004), assuming rapid equilibrium approximation for calcium buffers in various compartments:

$$\frac{dCa_i}{dt} = Ca_{Buf,c}\left[-\frac{I_{CaL,Ca} + I_{CaT} + I_{PMCA} + I_{bCa} - 2I_{NCX}}{2V_cF} + J_{Rel} - J_{up} + J_{leak}\right] \quad (3)$$

$$\frac{dCa_{SR}}{dt} = Ca_{Buf,SR} * \frac{V_c}{V_{SR}}\left(-J_{Rel} + J_{Up} - J_{leak}\right) \quad (4)$$

$$Ca_{Buf,X} = \frac{1}{1+\frac{Buf_{X*}K_{Buf,X}}{([Ca]_X+K_{Buf,X})^2}}\text{, for X=Cytoplasm (C), Sarcoplasmic Reticulum (SR)} \quad (5)$$

$$\frac{dNa_i}{dt} = -\frac{I_{Na} + I_{f,Na} + I_{CaL,Na} + I_{bNa} + 3I_{NCX} + 3I_{NaK}}{V_cF} \quad (6)$$

$$\frac{dK_i}{dt} = -\frac{I_{Kr} + I_{Ks} + I_{K1} + I_{to} + I_{f,K} + I_{CaL,K} - 2I_{NaK} + I_{stim}}{V_cF} \quad (7)$$

Where F is the Faraday constant, V_C is the cytoplasmic volume, V_{SR} is the sarcoplasmic reticulum volume, Buf_X is the total buffer concentration in a given compartment, and $K_{Buf,X}$ is the half-saturation constant of the buffer in a given compartment. Total volume and cytoplasmic buffering constants in the iPSC-CM model were set to experimental

measurements in iPSC-CMs from (V_{total}= V_C +V_{SR} =3960μm^3, Buf_C=0.06mM, and $K_{Buf,C}$ =0.0006mM) (Hwang *et al.*, 2015). Remaining SR buffering parameters (Buf_{SR}, $K_{Buf,SR}$) were optimized in the whole-cell optimization (Step 2). Relative proportions of volumes (V_C:V_{SR}), were retained from the adult human ventricular model by ten Tusscher et al. (ten Tusscher *et al.*, 2004), referred to as the ten Tusscher 2004 model. Capacitance of the cell was set to 60pF, based on the experimentally observed range in iPSC-CMs (18-89 pF) (Ma *et al.*, 2011; Hwang *et al.*, 2015; Li *et al.*, 2017).

The models were implemented in MATLAB version R2017a by The MathWorks Inc. and solved using ode15s.

Action Potential (AP) Morphology:

Action potentials (APs) in the baseline model and populations were evaluated by computing a series of AP morphology markers. Maximum diastolic potential (MDP) was the most negative voltage during the AP. Maximal upstroke velocity (dV/dt_{max}) was the maximal slope between two points in the computed AP upstroke. AP amplitude (Amp) was calculated as the difference in voltage between MDP and the peak voltage during the AP. AP duration (APD_x) was the time between dV/dt_{max} and X% AP repolarization from the peak voltage (ex. For APD_{90}, time from dV/dt_{max} to V_m =Peak - 0.9*Amp).

Parameter optimization of reformulated ionic channel models (Fig. 2, Step 1b):

For each of the reformulated currents, model parameters were optimized to multiple experimental datasets, resulting in dataset-specific parameterization instances of the model. For each dataset-specific model, external ion concentrations and voltage protocols were set to reflect the corresponding experimental conditions. Experimental conditions for each dataset are described in Table 1. All experimental data used to optimize the models was collected in iCell iPSC-CMs at physiological temperature (37^{o}C), unless otherwise specified (in which cases, data were temperature-corrected with appropriate Q_{10} values, as specified in the results section for the corresponding ionic current). This process was used to generate dataset-specific models. As an example, consider three separate experimental iPSC-CM datasets for a given current: datasets A, B, and C. In the case of the sodium current (Fig. 3), this would refer to (A) Ma et al., (B) Jalife Immature, (C) Jalife Immature.

Considering gating variable x in Fig. 1, parameters $x_{1\text{-}5}$ were optimized to recapitulate the experimental kinetics for gate x. In Fig. 2, this is shown as Step 1b in the upper highlighted box indicating the optimization routine. Parameter optimization minimized the error between the model and experimental voltage-dependence of the steady-state and time constants of a

given gate. The error function was the sum of the log squared difference between the data and model fit, normalized to the size of the dataset. The 'fminsearch' function was used in MATLAB to implement Nelder-Mead minimization of the error function. Random small perturbations (<10%) were applied to resulting local minima, to improve data fit. The parameter fit with the minimal error function value after 100 perturbations was used as the optimal model fit to the data. This is a relatively simple approach which only requires standard MATLAB functions, allowing for additional datasets-specific models to be easily obtained and incorporated into the model in the future. Additionally, this approach has been previously utilized for optimization of more complex ionic current models and datasets (Moreno *et al.*, 2016). The ionic current models in this study were chosen to minimize the number of optimized parameters, thus this approach was sufficient to successfully fit the models to the datasets presented.

These simplified models also allow for a more physiological understanding of model parameterizations. The ionic current model parameters can be combined such that:

$$x_\infty = \frac{\alpha_x}{\alpha_x + \beta_x} = \frac{1}{1 + \frac{\beta_x}{\alpha_x}} = \frac{1}{1 + \frac{x_3 e^{V/x_4}}{x_1 e^{V/x_2}}} = \frac{1}{1 + x_6 e^{V/x_7}} \quad (8)$$

Where:

$$x_6 = \frac{x_3}{x_1}, \quad x_7 = \frac{1}{(\frac{1}{x_4} - \frac{1}{x_2})} \quad (9)$$

With this simplification, we can understand the parameter effect on the voltage dependence of steady-state behavior. The x_∞ function has a sigmoidal voltage-dependence which is characterized by the slope and V_{half}, where $x_\infty(V_{half}) = 0.5$. Using the parameter combinations shown in Eqn. 8, x_6 and x_7 are proportional to V_{half} and slope, respectively.

Constructing the average parameter set for reformulated currents (Fig. 2, Step 1c):

Consider parameter x_1 in any gating variable. The value of x_1 is determined through parameter optimization to an experimental dataset. If three experimental datasets (datasets A, B, and C) are used, then each dataset corresponds to a unique parameter value of x_1 (x_{1A}, x_{1B}, x_{1C}) in each dataset-specific model. The baseline model is composed of average parameters values for x_1, such that:

$$x_{1,avg} = \frac{x_{1A} + x_{1B} + x_{1C}}{3} \quad (10)$$

This is repeated for each parameter in the ionic current model. These averaged parameters ($x_{1\text{-}5,avg}$, $g_{x,avg}$) comprise an average model for each current. The baseline model for each current was constructed using the average model gating kinetics. The baseline model is the starting point to implement variability.

Constructing the parameter distributions for reformulated currents (Fig. 2, Step 1d):

To create a population of models that capture variability between the dataset-specific models, we created a distribution for each parameter in the reformulated currents. This distribution is centered at the baseline ionic current model value. Similar to our approach in selecting an optimization method (Fig. 2, Step 1b), the sampling method was chosen for simplicity and to allow for variation in a large number of parameters. While the range of variability was determined by the range of the experimental datasets used to in form the model, there is still insufficient data to accurately determine to distribution of data between these datasets (constructing the distribution of experimental data would require more data than the 2-5 datasets per ionic current used in this study). For simplicity we used a normal distribution of parameters, and randomly selected the parameter values in building the population of models.

For example, for each cell in the population of models the value of x_1 is randomly chosen from a normal distribution around $x_{1,avg}$. The normal distribution is created using $x_{1,avg}$ and the standard deviation of x_{1A}, x_{1B}, and x_{1C}, as described above. This same process is used to create a distribution for each parameter ($x_{1\text{-}5}$) in each model gating variable, and for the maximal conductance (g_x).

Optimization of the baseline whole-cell model (Fig. 2, Step 2):

The pre-optimized whole cell model is composed of average parameter sets for the reformulated currents combined with non-reformulated currents from existing models in the whole-cell model structure and geometry as described above. To tune parameters in non-reformulated currents, as well as calcium handling parameters which were not directly defined by experiments, we implemented an optimization of the whole-cell model. This is shown in Fig. 2, Step 2, the second highlighted optimization routine in the flowchart.

To optimize the whole-cell model, 'fminsearchbnd' function was used in MATLAB to implement Nelder-Mead minimization of the error function. This "bound" version of the Nelder-Mead algorithm was used to maintain the reformulated maximal conductances within

a ±20% range of $g_{x,avg}$ from the pre-optimized baseline model. The maximal conductance of the reformulated currents, maximal conductances and fluxes of the remaining currents, SR buffering constants, calcium-dependent inactivation in I_{CaL}, RYR rate constants, and NCX kinetic parameters were optimized to fit whole-cell behavior within the experimentally observed range for iPSC-CMs. As in the optimization of the ionic currents, the error function was defined as the sum of the log squared difference between the experimental data and whole-cell model output. The targets for the optimization function considered the experimentally observed range of AP morphology (MDP, APD_{90}, AP amplitude, maximal upstroke velocity), CaT morphology (time constant of decay, time to peak, ratio of tau decay and time to peak, CaT amplitude, and diastolic $[Ca^{2+}]$), calcium handling response to caffeine (peak calcium and decay, not shown) (Hwang *et al.*, 2015), and contribution of SERCA, NCX, and PMCA to calcium efflux from the cytosol.

The ionic current models shown as black lines in Fig. 3-9 are the final version of each current model, including all tuning of maximal conductance in the whole-cell optimization. The baseline model resulting from this optimization was used as the starting point for all subsequent populations. All parameters which were not randomized in the model populations (remaining currents, cell geometry, etc.) were kept at the baseline model values.

Sensitivity Analysis

To further analyze the baseline models (Fig. 11E, 15C), parameter sensitivity was conducted using multivariable linear regression (Sobie, 2009). Sensitivity analysis was conducted based on variation of the maximal conductance and maximal ion transport rates of the transmembrane currents (I_{Na}, I_{CaL}, $I_{CaT,}$ I_{Kr}, I_{Ks}, I_{K1}, I_{to}, I_f, I_{NCX}, I_{NaK}, I_{PMCA}, I_{bNa}, and I_{bCa}) and SR fluxes (J_{Up}, J_{Rel}, and J_{leak}). Remaining parameters, including all parameters describing model kinetics, were held at the baseline model values. Random scaling factors and were chosen from a log-normal distribution with a median value of 1, standard deviation of 0.1. 5000 randomly parameterized models were run for each sensitivity analysis shown. For the baseline population (Fig, 11E, immature 15C) only spontaneously beating, AP generating, models were analyzed. This resulted in 89.3% model retention rate. For the mature population, only stimulated beating, AP generating, models were analyzed. This resulted in 67.2% model retention rate. For each analysis shown, 50 randomly determined subpopulations of 1000 models was analyzed, resulting in a standard deviation of less than 0.025 for all regression bars shown. Each cell simulation was run until there was a <1% change in minimum ion concentration (for Ca_i, Ca_{SR}, Na_i, and K_i) between the first and last beat during a 50 second simulation run. Once the steady-state criteria were met (ranging from 60-600s), the final AP was saved for regression analysis.

Development of population-based models based on experimental variability (Fig. 2, Step 3):

To create a population of models (as shown in Fig 12, 13, and 16), the parameters of the varied currents were randomly determined using the parameter distributions created from the dataset-specific models. Each parameter was chosen from a distribution centered at the baseline model value. For example, for each cell in the population of models the value of x_1 is randomly chosen from a normal distribution around $x_{1,avg}$. The normal distribution is created using $x_{1,avg}$ and the standard deviation of x_{1A}, x_{1B}, and x_{1C}, as described above (Fig. 2, Step 1c). This same process is used to create a distribution for each parameter (x_{1-5}) in each model gating variable, and for the maximal conductance (g_x). The populations are constructed by randomly selecting each parameter from these distributions. In the single-current variation populations, all parameters for the chosen current are randomly determined, and the remaining model currents retain the baseline model formulation. In the final population, parameters for all 5 varied currents (I_{Na}, I_{CaL}, I_{Kr}, I_{K1}, and I_f) are randomly selected from the constructed distributions.

Experimental Calcium Imaging (Wu Lab):

iPSC-CMs were disassociated by Accutase and seeded in Matrigel-coated (BD bioscience) coverslips at a density of 20,000 cells per well. After recovery, cells were loaded with 5μM Fura-2 AM in Tyrode's solution (140mM NaCl, 5.4 mM KCl, 1 mM MgCl2, 10 mM glucose, 1.8 mM CaCl2, and 10 mM HEPES pH = 7.4 with NaOH at RT) for 10 minutes in incubator, and were washed with pre-warmed Tyrode's solution for 3 times afterward. Cells were paced at 0.5 HZ during recording. For Fura-2 AM imaging, calcium signals were sampled by custom-made Nikon Eclipse Ti-E inverted microscope with a 40× oil immersion objective (NA 0.95) and Lambda DG-4 ultra-high speed wavelength switching light source (Sutter Instrument). Signals were collected with iXon Ultra 897 EMCCD (Andor) as high-frame-rate video (512X512, 50 fps). Custom-made IDL (interactive digital language) script was used for data analysis. Calcium signal intensity was expressed F340/380 in Fura-2 AM recording. For each cell line, we recorded at least 30 cells from 2 batches of differentiation.

Experimental Electrophysiology Recordings (Kurokawa Lab):

Methods for I_{K1}, I_{Na}, and I_f experimental data used to optimize the model is as described previously in Li et al. Methodology for I_{CaT} recordings are described here.

Cell culture (Kurokawa Lab): We used commercially available human iPS cell (hiPSC)-derived cardiomyocytes, iCell-cardiomyocytes (Cellular Dynamics International Japan; CDIJ, Tokyo, Japan). Pre-cultured iCell-cardiomyocytes obtained according to the company manual were dissociated enzymatically and were cultured onto laminin/poly-D/L-lysine-coated glass bottom dishes. These re-plated cells started to beat within 48 hours. Electrophysiological experiments were performed within 2 weeks after thawing, as the distributing company (CDIJ) warrants preservation of a high purity in the user's guide.

Electrophysiology (Kurokawa Lab): Membrane currents were recorded with the perforated configuration of the patch-clamp technique using an Axopatch 200B amplifier (Molecular Devices, CA, USA). Signals were low-pass filtered at 5 kHz, and sampled at 2–5 kHz. No correction for the liquid junction potential was made. The pCLAMP software (version 9.2 or 10.02) was used to generate voltage-pulse protocols, and for acquisition and analysis of data.

Cultured cells were placed on the stage of the inverted microscope (IX-71, Olympus), and the culture medium was replaced by a Tyrode's solution (135 mM NaCl/ 0.33 mM NaH_2PO_4/ 5.4 mM KCl/ 1.8 mM $CaCl_2$/ 0.53 mM $MgCl_2$/ 5.5 mM glucose/ 5 mM HEPES, pH 7.4). After the giga-ohm seal formation, the Tyrode's solution was replaced to the external recording solution for each membrane current by using a rapid perfusion system (time constant; >20 ms) (Kurokawa *et al.*, 2001). Each patch-clamp data was obtained from an individual culture dish. Experiments were performed at 36±1 ^{o}C.

During recordings of $I_{Ca,T}$, external Na^+ ions and all K^+ ions were replaced by tetraethyl ammonium $(TEA)^+$ and Cs^+ ions in order to suppress both Na^+ currents and K^+ currents. Pipette solution contained (130 mM CsCl/ 20 mM TEACl/ 2 mM $MgCl_2$/ 5 mM ATP-2Na/ 10 mM HEPES/ 10 mM EGTA, pH 7.25), supplemented with amphotericin B. To achieve patch perforation, we front-filled patch pipettes by dipping them into the internal solution, and back-filled with the internal solution containing amphotericin B. Adequate series resistances (less than 5-times of the pipette resistances) were usually attained within 10 min after the gigaohm seal formation. Each current component was determined in each single cell by subtracting the traces after application of channel blocker. Our rapid perfusion system

enables us to exchange the bath solution almost immediately, that minimize the risk for contamination of time-dependent leak currents.

After the achievement of membrane perforation, the Tyrode's solution was replaced by a Na^+-free K^+-free solution (135 mM TEACl/ 5.4 mM CsCl/ 2 mM $CaCl_2$/ 0.53 mM $MgCl_2$/ 11 mM glucose, 5 mM HEPES, pH 7.4). TTX at 10 μM was added to the solution in order to abolish contamination with low-threshold activating TTX-sensitive Ca^{2+} currents (Vassort *et al.*, 2006). According to a comparison of current-voltage (I-V) relationships from -100 mV and -50 mV, $I_{Ca,T}$ currents were elicited by 150-ms test pulses to -30 mV (V_H of -100 mV, 0.1 Hz). The obtained inward currents were completely blocked with 0.5 mM $NiCl_2$ (data not shown), representing most of the $I_{Ca,T}$ component. Two representative data points were referred to for optimization of the model.

RESULTS:

We set out to develop a computational model that can recapitulate the varied electrophysiological responses of induced pluripotent stem cell-derived cardiomyocytes (iPSC-CMs). A schematic of the model cell containing all the ionic processes and compartments in the model is shown in Fig. 1. All major ionic currents (indicated by red stars in Fig. 1) were formulated and parameterized to fit iPSC-CM experimental kinetic data.

Sodium Current (I_{Na}):

The sodium current model contains three Hodgkin-Huxley type gating variables: activation (m), fast-inactivation (h), and slow-inactivation (j), as described previously (Beeler & Reuter, 1977). The model formulation for the sodium current is shown as the example current in Fig. 1. For each gating variable, experimental data from iPSC-CMs was used to optimize model parameters (x_{1-5}). Three distinct dataset-specific models of the sodium current were optimized, based on three independent experimental datasets. One sodium dataset was from Ma et al. (Ma *et al.*, 2011), and two independent datasets were from the Jalife Lab (Herron *et al.*, 2016). The immature dataset from the Jalife Lab was collected in iPSC-CMs plated on glass coverslips (conventional cell preparation). The mature dataset from the Jalife Lab was collected in iPSC-CMs plated on PDMS (polydimethylsiloxane) coverslips, which were shown to promote mature electrophysiological function in iPSC-CMs (Herron *et al.*, 2016). The Jalife Lab data was collected at room temperature. Before optimizing the model

parameters, the Jalife Lab experimental data was converted to physiological temperature using Q_{10}=2.79 for time constants (ten Tusscher *et al.*, 2004) and Q_{10}=1.5 for conductance (Correa *et al.*, 1991). Experimental data shown in Fig. 3C-D is adjusted data to physiological temperature. Experimental iPSC-CM voltage dependence of steady-state inactivation and activation data were used to optimized parameters for $h_\infty * j_\infty$ and m_∞^3, respectively. The experimental data used for parameterization, and the resulting models, are shown in Fig. 3A.

Several experimentally published datasets from iPSC-CMs do not contain explicit information for the time constants of gating processes. However, current recording traces were published. To extract time constants of gating kinetics, normalized current recordings from published data were fit to single-exponential functions ($e^{-t/\tau}$; t=time, τ =time constant) for activation and/or inactivation at each voltage step. These extracted time constant values were used to optimize model parameters. In the sodium current, this technique was used to extract activation and fast-inactivation time constants from sodium current recordings in Ma et al. and Herron et al. The resulting time constant values (corrected to physiological temperature), and respective model fits are shown in Fig. 3C-D. All three dataset-specific models were optimized to data from the Kurokawa Lab for time constants of slow-inactivation, as shown in Fig. 3E. The maximal conductance for each model was tuned to fit the I-V relationship for the corresponding dataset, as shown in Fig. 3B. The sodium current kinetics in the baseline iPSC-CM model are shown in black (Fig. 3).

L-type Calcium Current (I_{CaL}):

The model L-type calcium current contains voltage-dependent activation and inactivation gating variables (x_{act}, x_{inact}). Both gates were modeled using the formulation shown for example gate x in Fig. 1. The model also includes a calcium-dependent inactivation gate ($x_{inact,Ca}$) from the ten Tuscher 2004 model. The model L-type calcium current is described by:

$$I_{CaL,y} = p_{CaL,y} * x_{act} * x_{inact} * x_{inact,Ca} * z_y^2 * \frac{VF^2}{RT} \gamma_y \frac{[Y]_i e^{z_y VF/RT} - [Y]_o}{e^{z_y VF/RT} - 1} \qquad (11)$$

Where y is Ca^{2+}, Na^+, or K^+. $p_{CaL,y}$ indicates the permeability to ion y, R is the gas constant, z_y is the valence of ion y, and γ_y is to activity coefficient for ion y as in the Shannon-Bers model. The total current is the sum of the Ca^{2+}, Na^+, and K^+ currents.

$$I_{CaL} = I_{CaL,Ca} + I_{CaL,Na} + I_{CaL,K} \qquad (12)$$

Parameters for the voltage-dependent inactivation and activation gates (x_{inact} and x_{act}) were optimized to iPSC-CM experimental steady-state inactivation and activation curves, as well as voltage-dependent time constants of inactivation and activation. The four dataset-specific

models were optimized to experimental data from Ma et al., Es-Salah-Lamoureux et al., and two independent datasets from Veerman et al. (Ma *et al.*, 2011; Es-Salah-Lamoureux *et al.*, 2016; Veerman *et al.*, 2016). Es-Salah-Lamoureux et al. and Veerman et al. used an in-house iPSC-CM line for experimental results shown. Ma et al. and Es-Salah-Lamoureux et al. I_{CaL} recordings were conducted at room temperature and converted to physiological temperature using Q_{10}=2.1 for time constants (ten Tusscher *et al.*, 2004), and Q_{10}=2.3 for conductance (Kiyosue *et al.*, 1993).

Steady-state inactivation and activation iPSC-CM experimental data, and optimized dataset-specific models for each dataset, are shown in Fig. 4A. Due to a lack of explicitly reported experimental iPSC-CM data for the time constants of voltage-dependent L-type calcium gating, time constants were extracted from Ma et al. current recordings (as described above for the sodium current). The Ma et al. time constants, corrected to physiological temperature, were used to optimize all models. The experimental conditions for calcium buffering during the Ma et al. I_{CaL} current recordings (5 mM EGTA), may result in some calcium-dependent inactivation contribution to the time constants of inactivation derived from these current recordings. As this calcium-dependent inactivation contribution was not quantified experimentally, the time constants of inactivation derived from the current recordings were assumed to be entirely voltage-dependent inactivation for model parameterization. The time constant data used for model optimization, and the resulting models, are shown in Fig. 4C-D.

The calcium-dependent inactivation gate ($x_{inact,Ca}$) formulation in the ten Tusscher 2004 model was retained in this model, due to lack of experimental data characterizing calcium-dependent inactivation in iPSC-CMs. A single scaling factor for $[Ca]_i$ in $x_{inact,Ca,\infty}$ was optimized in the final whole-cell parameter optimization to recapitulate iPSC-CM calcium handling. This was required to accommodate the lower $[Ca]_i$ throughout the iPSC-CM AP, as compared to the adult ventricular cell modeled in ten Tusscher 2004. Fig. 4 shows all I_{CaL} models with the final optimized calcium-dependent inactivation gate.

Values for γ_{Ca}, γ_{Na}, γ_K, and the relative proportions of $p_{CaL,Ca}$: $p_{CaL,Na}$:$p_{CaL,K}$ were retained from the Shannon-Bers model (Shannon *et al.*, 2004). The total permeability (p_{CaL} = $p_{CaL,Ca}$+ $p_{CaL,Na}$ + $p_{CaL,K}$) of each dataset-specific model was tuned using the experimental I-V curves, and the resulting I-V relationships are shown in Fig. 4B. The baseline model for I_{CaL} is shown in black in Fig. 4.

T-type Calcium Current (I_{CaT})

The T-type calcium current was introduced to the iPSC-CM model, as it is experimentally found in iPSC-CMs. T-type calcium is typically found in embryonic hearts, and its expression is dependent on the developmental stage of the heart (Ono & Iijima, 2010). T-type calcium is also found experimentally in iPSC-CMs (Ivashchenko *et al.*, 2013; Karakikes *et al.*, 2015), as is expected due to the iPSC-CMs immature cardiac phenotype. The T-type calcium current was modeled as in the previously published Maltsev-Lakatta sinoatrial node model (Maltsev & Lakatta, 2009). Peak I_{CaT} was tuned to the IV curves for I_{CaT} provided by the Kurokawa Lab, as shown in Fig. 4E.

Rapid Delayed Rectifier Potassium Current (I_{Kr})

The rapid delayed rectifier potassium current was modeled as:

$$I_{Kr} = g_{Kr} * \sqrt{\frac{K_0}{5.4}} * x_{act} * x_{inact} * (V_m - E_K) \quad (13)$$

The voltage-dependent activation and inactivation gating variables (x_{act}, x_{inact}) were modeled using the formulation shown as for the exemplar gate x in Fig. 1. The K_o dependence of the current ($\sqrt{K_o/5.4}$) and the voltage-dependent inactivation gate was retained from the ten Tusscher 2004 formulation of I_{Kr}. To utilize the simplified gating model formulation for the I_{Kr} inactivation gate (x_{inact}), the single-exponential voltage-dependent rate constant model (Fig. 1, right) was optimized to fit the voltage-dependence of I_{Kr} inactivation in the ten Tusscher 2004 model. The resulting model of inactivation gating is shown in Fig. 5A,D.

Dataset-specific models of steady-state activation were fit to four independent iPSC-CM experimental datasets from the Wu Lab, Ma et al., Es-Salah-Lamoureux et al., and Bellin et al. (Ma *et al.*, 2011; Bellin *et al.*, 2013; Es-Salah-Lamoureux *et al.*, 2016; Garg *et al.*, 2018). Es-Salah-Lamoureux et al. data was collected from an in-house iPSC-CM line, and Bellin et al. data was collected from a patient-specific cell line. Voltage-dependent time constants of activation were extracted from current recordings published in Ma et al. The Ma et al. time constants of activation were used to optimize parameters in the Ma et al., Wu Lab, and Es-Salah-Lamoureux et al. optimized models. Experimental time constants of activation were published in Bellin et al. and used in the corresponding model, as shown in green in Fig. 5C. Finally, the maximal conductance (g_{Kr}) of each dataset-specific model was tuned to I-V relationship data for each dataset, shown in Fig. 5B. Bellin et al. published a single data point for the experimental I-V relationship (at V_m=60mV, not shown), which was used to optimize the maximal conductance of the corresponding model.

Transient outward potassium current (I_{to})

The transient outward potassium current was modeled as:

$$I_{to} = g_{to} * x_{act} * x_{inact} * (V_m - E_K) \quad (14)$$

The voltage-dependent activation and inactivation gating variables (x_{act}, x_{inact}) were modeled using the formulation of example gate x in Fig. 1. iPSC-CM experimental data from Ma et. al., Cordeiro et al., and Veerman et al. was used to optimize dataset-specific models (Ma *et al.*, 2011; Cordeiro *et al.*, 2013; Veerman *et al.*, 2016). Experimental results in Veerman et al. were recorded in an in-house iPSC-CM cell-line. Steady-state activation and time constants of inactivation were extrapolated from I_{to} current recordings published in Ma et al. Time constants of inactivation from Ma et al. were used to optimize the inactivation time constant parameters of the Veerman et al. model. Steady-state activation data from Ma et al. was used to optimize the Cordeiro et al. model, and steady-state inactivation data from Cordeiro et al. was used to optimize the Ma et al. model, as neither dataset included both steady-state activation and inactivation data.

Time constants for activation of I_{to} were not available in iPSC-CMs, thus model parameters were optimized to retain the ten Tusscher 2004 voltage-dependence for time constants of activation. The resulting model for time constants of I_{to} activation are shown in Fig. 6C. Finally, maximal conductance (g_{to}) was tuned to experimental iPSC-CM I-V relationships for each dataset, as shown in Fig. 6B.

Slow Delayed Rectifier Potassium Current (I_{Ks})

The slow delayed rectifier potassium current was modeled as:

$$I_{Ks} = g_{Ks} * x_{act}^2 * (V_m - E_K) \quad (15)$$

The voltage-dependent activation gating variable (x_{act}) was modeled using the formulation of example gate x in Fig. 1. Dataset-specific models were optimized to experimental data from Ma et al. (2011) and two independent datasets from Ma, Wei et al. (2015), shown in Fig. 7A (Ma *et al.*, 2011; Ma *et al.*, 2015). Ma, Wei et al., recorded one I_{Ks} dataset in a patient-specific iPSC-CM cell-line, and another dataset in iCell iPSC-CMs. Parameters for $x_{act,\infty}^2$ were optimized to steady-state activation data, as shown in Fig. 7A. Due to a lack of available experimental data for the time constants of I_{Ks} activation, time constants extracted from current recordings published in Ma et al. were used to optimize parameters in all models, as shown in Fig. 7B. Finally, the maximal conductance (g_{Ks}) was tuned to I-V data, as shown in Fig. 7C. For both models built on Ma, Wei et al. datasets (Fig. 6: patient-specific in orange, iCell in purple), the maximal conductance was tuned to the Ma, Wei et al. (2015) IV relationship in iCells, as shown by purple points in Fig. 7C.

Pacemaker/Funny Current (I_f)

The pacemaker current was incorporated into the iPSC-CM model, as it is experimentally found in iPSC-CMs (Karakikes *et al.*, 2015; Kim *et al.*, 2015). The current was formulated as:

$$I_f = g_F * x_{act} * (V_m - E_f) \quad (16)$$

E_f and g_f are calculated as a balance of the sodium and potassium Nernst potentials (Verkerk & Wilders, 2013), such that :

$$g_f(V_m - E_f) = g_{f,Na}(V_m - E_{Na}) + g_{f,K}(V_m - E_K) \quad (17)$$

Where the ratio of $g_{f,Na}$:$g_{f,K}$ = 0.491, based on prior models of I_f in rabbit sinoatrial node (Verkerk & Wilders, 2013). The activation gate (x_{act}) is modeled using the same formulation as example gate x in Fig. 1. Experimental data in iPSC-CMs from Ma et al. and the Kurokawa Lab (Ma *et al.*, 2011; Li *et al.*, 2017) was used to optimize dataset-specific models. Model parameters for the activation gate (x_{act}) were optimized to experimental data for steady-state activation and time constants of activation, as shown in Fig. 8A-B. Maximal conductances (g_f) for each dataset-specific model were fit to I-V relationships of the corresponding experimental dataset. The experimental data and resulting models are shown in Fig. 8C.

Inward Rectifier Potassium Current (I_{K1})

The slow delayed rectifier potassium current was modeled as:

$$I_{K1} = g_{K1}\sqrt{\frac{K_0}{5.4}} * x_{act,\infty} * (V_m - E_K) \quad (18)$$

The K_o dependence of the current ($\sqrt{K_o/5.4}$) is retained from the ten Tusscher 2004 formulation of I_{K1}. To recapitulate the behavior of I_{K1} the activation gate was formulated as:

$$\alpha_x = x_1 e^{(V+x_3)/x_2} \quad (19)$$

$$\beta_x = e^{(V+x_5)/x_4} \quad (20)$$

Dataset-specific models were created by optimizing parameters $x_{1\text{-}5}$ and g_{K1} to the I-V relationships recorded in iPSC-CMs from Ma et al., Kurokawa Lab, and Jalife Lab (Ma *et al.*, 2011; Herron *et al.*, 2016; Li *et al.*, 2017). Experimental data from the Jalife Lab was collected at room temperature. The Jalife Lab I-V curves were corrected to physiological temperature using Q_{10}=1.5 (Kiyosue *et al.*, 1993). The experimental data used to optimize the models, and the resulting models, are shown in Fig. 9.

Pump and Exchanger Currents (I_{NCX}, I_{NaK}, I_{PMCA}***):***

To model the remaining membrane currents which are not characterized in iPSC-CMs, we utilized previous models. The sodium-calcium exchanger (I_{NCX}), sodium potassium pump (I_{NaK}), and sarcolemma pump (I_{PMCA}) currents were modeled using formulations from prior

ventricular cell models (Luo & Rudy, 1994; ten Tusscher *et al.*, 2004). Kinetics of these currents were retained from existing ventricular cell models, as these currents have not been characterized experimentally in iPSC-CMs. Maximal values of all three currents were included in the whole-cell optimization routine (Fig. 2, Step 2), and the final parameterizations are detailed in Table 3.

$$I_{NCX} = k_{NCX} * \frac{\left(e^{\gamma VF/RT} * {[Na]_i}^3 * [Ca]_o\right) - \left(e^{\frac{(\gamma-1)VF}{RT}} * {[Na]_o}^3 * [Ca]_i * \alpha\right)}{\left({K_{mNa}}^3 + {[Na]_o}^3\right) * (K_{mCa} + [Ca]_o) * \left(1 + k_{sat} * e^{\frac{(\gamma-1)VF}{RT}}\right)} \quad (21)$$

$$I_{NaK} = \frac{P_{NaK} * [K]_o * [Na]_i}{([K]_o + K_{mK}) * ([Na]_i + K_{mNa}) * \left(1 + 0.1245 * e^{\frac{-0.1*VF}{RT}} + 0.0353 * e^{\frac{-VF}{RT}}\right)} \quad (22)$$

$$I_{PMCA} = g_{PMCA} * \frac{[Ca]_i}{([Ca]_i + K_{PMCA})} \quad (23)$$

Sarcoplasmic Reticulum (SR) Currents (J_{Rel}, J_{up}, J_{leak}):

The calcium handling in iPSC-CMs has not been fully characterized experimentally. Thus, the calcium handling in the present model is based on prior formulations of SR currents. Parameters for the RYR (J_{rel}) were adapted from the Shannon-Bers model to maintain physiological SR function during the beating cycle. The Shannon-Bers RYR formulation is dependent on the high calcium concentration in the cleft compartment described in the Shannon-Bers cellular geometry. However, the geometry used in the present model does not include this cleft compartment (as shown in Fig. 1 schematic). Given these differences in cellular geometry, the original Shannon-Bers J_{Rel} parameters do not produced a SR release during the AP in the simplified cellular geometry used in this model. To implement the Shannon-Bers RYR Markov model formulation within the cellular geometry described above, RYR transition rates were determined by our whole-cell optimization routine (Fig. 2, Step 2). Maximal values of J_{up} and J_{leak} were also included in the whole-cell optimization. Final parameterizations of all SR currents are detailed in Table 3.

$$J_{up} = \frac{V_{max,up}}{\left(1 + \frac{{K_{up}}^2}{{[Ca]_i}^2}\right)} \quad (24)$$

$$J_{leak} = V_{leak} * ([Ca]_{SR} - [Ca]_i) \quad (25)$$

For Closed (C), Open (O), Inactivated (I), Closed- inactivated (CI) states of J_{Rel}:

$$CI = 1 - C - O - I \quad (26)$$

$$\frac{dC}{dt} = (k_{im} * CI - k_{iSRCa} * [Ca]_i * C) - (k_{oSRCa} * [Ca]_i^2 * C - k_{om} * O) \quad (27)$$

$$\frac{dO}{dt} = (k_{oSRCa} * [Ca]_i^2 * C - k_{om} * O) - (k_{iSRCa} * [Ca]_i * O - k_{im} * I) \quad (28)$$

$$\frac{dI}{dt} = (k_{iSRCa} * [Ca]_i * O - k_{im} * I) - (k_{om} * I - k_{oSRCa} * [Ca]_i^2 * CI) \quad (29)$$

$$J_{Rel} = k_s * O * ([Ca]_{SR} - [Ca]_i) * \frac{V_{SR}}{V_C} \quad (30)$$

Model development: Intracellular Ca^{2+} dynamics

Fig. 10A shows the baseline model (red) calcium transient compared to experimental calcium transients (CaTs) from the Wu Lab (grey). Experimental CaTs shown are reported as a florescence ratio (F_{ratio}), as plotted in Fig. 10A on the right y-axis. The average peak F_{ratio} value of the dataset shown (Peak F_{ratio} = 4.25), corresponds to the independently measured iPSC-CM average peak CaT concentration (Fig. 10B) on the left y-axis. Similarly, the diastolic F_{ratio} value (Diastolic F_{ratio} = 0) also corresponds to the independently measured iPSC-CM average diastolic CaT concentration (Fig. 10B).

To reproduce the CaT data described above, SR currents (J_{Up}, J_{Rel}, and J_{leak}) and calcium-dependent transmembrane currents which were not previously parameterized to fit iPSC-CM data (I_{NCX}, I_{PMCA}) were optimized to recapitulate the experimentally observed iPSC-CM CaT morphology shown in Fig. 10B. The baseline model parameters were optimized to produce CaT outputs within one standard deviation of the experimental Ca^{2+} transient markers shown. Additionally, the optimization considered the ratio of time to peak and tau decay of the CaT. The baseline model has a faster spontaneous beating rate (62.0 bpm) than the average spontaneous beating rate in the CaT dataset from the Wu Lab (30.2 ± 13.2 bpm). To normalize the experimental data and account for this difference in pacing rate, we included the ratio of the CaT time to peak and CaT tau decay as a target in our optimization error function. The ratio of the time to peak and tau decay of the experimental CaT was 0.83, and the resulting baseline model CaT ratio is 0.77. Thus, the model recapitulates the relative portion a single AP cycle spent at each phase of the CaT.

The model was also tuned to recapitulate the relative contribution of three fluxes (I_{NCX}, J_{Up}, and I_{PMCA}) to the calcium removal pathways (Fig. 10C and D) (Hwang *et al.*, 2015). Experimentally, the contribution of NCX (I_{NCX}), SERCA (J_{Up}), and the sarcolemma pump (I_{PMCA}) is calculated using the time constant of the CaT during a normal AP, the caffeine-induced CaT, and the caffeine-induced CaT in a sodium and calcium-free solution (Bers, 2000). Hwang et al. provided a comparison of the relative contributions I_{NCX}, J_{Up}, and I_{PMCA} to

the calcium flux balance from 6 independent iPSC- CM datasets across 3 labs (Hwang *et al.*, 2015). Maximal I_{NCX}, J_{Up}, and I_{PMCA} in the baseline model were optimized to fit the relative contributions of each current. The relative contribution to the calcium flux in the model was calculated based on the integral of each current during a single CaT. This integral, normalized to total calcium contribution from all three sources, is shown in Fig. 10C for a single beat in the baseline model, obtained after achieving steady-state. The resulting relative contributions to calcium flux pathways in the model are comparable to the experimentally observed ranges (Fig. 10D).

Model Prediction: Whole Cell Simulations

The baseline model that was developed via the steps described above recapitulates the phenotype of typical iPSC-CMs (Fig.11A). The AP and CaT outputs fall within the experimental range of behaviors (Fig. 10-11). Experimental details of the action potential datasets used are described in Table 2. The baseline model was optimized to reproduce these key features of the immature iPSC-CM phenotype, including spontaneous beating (Fig. 11A&C), a reduced AP amplitude (Fig. 11B), a low maximal upstroke velocity (Fig. 11C), and a depolarized maximum diastolic potential (MDP, Fig. 11D). See methods for precise definitions of AP morphology markers. The baseline model also spontaneously beats during total I_{Na} and I_f block, showing that the mechanism of automaticity in the baseline model is consistent with the experimentally observed mechanism (Guo *et al.*, 2011; Itzhaki *et al.*, 2011; Sheng *et al.*, 2012; Kim *et al.*, 2015). Sensitivity analysis on the baseline model was conducted using a multivariable regression model (Fig. 11E) (Sobie, 2009). The sensitivity analysis shows several expected results for cardiac cells such as increased upstroke velocity with increased sodium current, APD shortening with increased I_{Kr}, and APD lengthening with increased I_{CaL}. Additionally, increased I_{K1} is experimentally shown to hyperpolarize iPSC-CM maximum diastolic potential (Bett *et al.*, 2013; Vaidyanathan *et al.*, 2016), which is consistent with the results of this sensitivity analysis (Fig. 11E) showing increased I_{K1} hyperpolarizes the cells (indicated by a positive regression coefficient for I_{K1} related to the absolute value of MDP).

While Fig. 11B-D shows that the baseline model falls within the experimental range, the compilation of experimental data sources also serves to illustrate the vast range of AP behavior in "normal" iPSC-CMs. This range of experimentally observed behaviors reveals that a single "average" iPSC-CM model is insufficient to describe the behavior of iPSC-CMs, and that variability may be the defining characteristic.

Model Prediction: Inter-subject Variability

To model heterogeneity in kinetic behavior in healthy iPSC-CMs, a population-based approach was utilized. The goal of this approach was to harness the range of experimentally observed kinetics in each ionic current and create an *in silico* population of model cells which captured the full range of iPSC-CM kinetic behavior.

A population of models was developed to incorporate experimentally measured kinetic variability in five of the reformulated ionic currents that were identified in the multivariable regression sensitivity analysis as most important to AP behavior (Fig. 11E). The 5 currents were I_{Na}, I_{CaL}, I_{Kr}, I_f, and I_{K1}. The regression coefficients for I_f were below the threshold for Fig. 11E, but I_f did impact MDP and BPM in the model, though at a lower level than the other currents shown in Fig. 11E. I_{NaK} was identified by the sensitivity analysis, but due to the lack of experimental iPSC-CM data characterizing the range of kinetic behavior in I_{NaK}, it was not included in the population-based variability.

A total of six populations were developed. In five of those populations, model parameters for a single current were varied, and all other currents were kept at the baseline values. The populations capture inter-subject variability observed in the measured electrophysiology data. In the final population, the parameters were simultaneously varied for all five of the identified currents.

To simulate model cell variability, ionic current models were randomly parameterized within the experimentally observed ranges from multiple data sets for steady-state gating, time constants of gating, and IV relationships. Using the mean and standard deviation of each parameter value across the independent dataset-specific models, a normal distribution was created for each parameter value, as described in further details in the methods and Fig. 2. For each model cell within the population, parameters were randomly chosen from this distribution. Thus, every model cell in the population has a unique parameter-set chosen from the normal distribution of underlying parameters composing a single current. The range of kinetic behaviors are shown for populations with single current variation in I_{Na} (Fig. 12A), I_{CaL} (Fig. 12B), I_{Kr} (Fig. 12C), I_f (Fig. 12D), and I_{K1} (Fig. 12E). Steady-state and time constant values functions shown in Fig. 12 are the results of random variation in the parameter values of each of the selected five currents. These randomly determined kinetics result in the whole-cell behavior shown in Fig. 13.

A final population was built using the same methodology, but by varying the kinetics of the five specified currents simultaneously (shown as effects on the AP in blue in Fig. 13). The outputs of the spontaneously beating AP models from the single-current variation

populations are shown in Fig. 13A, and the spontaneously beating AP generating models from the five-current simultaneously varied population is shown in Fig. 13B. Each cell in the resulting populations can be categorized into one of three groups: spontaneously beating cells, stimulated beating cells, or cells excluded from analysis. “Spontaneously beating cells” maintain automaticity with a viable AP and are most representative of the experimentally observed iPSC-CMs. The baseline model would be categorized in the spontaneous beating subpopulation. “Stimulated beating cells” are model cells that result in a viable AP with the application of a stimulus current but are non-spontaneously beating (not shown). Cells were not analyzed if they did not fully repolarize (MDP>-40 mV, AP amplitude < 70 mV) or exhibited non-control/non-healthy AP morphology (e.g. alternans). Additionally, cells with non-physiological calcium handling (determined as CaT amplitude greater than three standard deviations of the experimental average in Fig 10B) were excluded from analysis

For the cell population subject to single-current variation, only the I_{K1} variation population produced a stimulated beating subpopulation that required an external stimulus. A random selection of models from the spontaneously beating AP generating populations are shown in Fig. 13C, to illustrate the range of beating rates and AP morphologies observed. All subsequent analyses were conducted in the subpopulation generating spontaneously beating APs. Variation in AP morphology markers within each population of models is shown in Fig. 13D-G. Individual colored points in Fig. 13D-F represent a single model in the given population. Additionally, these outputs are compared to experimentally measured iPSC-CM outputs shown as black dots and lines (Ma *et al.*, 2011; Doss *et al.*, 2012; Cordeiro *et al.*, 2013; Ma *et al.*, 2015; Es-Salah-Lamoureux *et al.*, 2016; Herron *et al.*, 2016), as was done for the baseline model in Fig. 11. It should be noted that the plots show standard error for the experimental data, meaning the full range of experimental behavior is larger than represented by the black points. The range of individual models in the single-current variation populations can serve as a form of sensitivity analysis: for a given morphology marker, the widest spread of models is indicative of increased sensitivity to the varied current. For example, the maximal upstroke velocity is sensitive to I_{Na}, and thus the models from the I_{Na} varied population show the largest range of upstroke velocity values (Fig. 13F, distribution of green points along y-axis). Finally, the population with simultaneous variation of five ionic currents shows the largest range of variability in all AP morphology markers and is the population most representative of the full experimentally observed space. This serves as a first step in modeling known variability of iPSC-CMs at the ionic level, resulting in the recapitulation of observed variability in iPSC-CMs at the whole-cell level.

Model Prediction: Ionic Current Block

To further validate the model population, we predicted the effect of ionic current blockers on the model population. We simulated the effect of drugs which have been experimentally studied in iPSC-CMs: Tetrodotoxin (TTX, I_{Na} block), E-4031 (I_{Kr} block), and Nifedipine (I_{CaL} block). For each drug we simulated a concentration which had been studied across several experimental datasets. We modeled drug effects as a simple pore block. IC50 values for each cell in the population were randomly selected within the range of experimentally observed IC50 values in stem cell-derived cardiomyocytes (Peng *et al.*, 2010; Ma *et al.*, 2011; Harris *et al.*, 2013; Gibson *et al.*, 2014; Moreau *et al.*, 2017). The ranges of IC50 values, and corresponding percent ionic current block, are described in Table 4. For example, when modeling 10μM TTX, each model cell had a randomly determined IC50 within the experimental range, resulting in 88% - 94% I_{Na} block. Beginning at the previously determined control steady-state initial conditions, each simulation was run for 200s with drug applied, and the final action potential was analyzed. All simulated results shown are in spontaneously beating model cells. The percent change in the AP parameter associated with the blocked current is described in Table 4, and sample APs for each drug are shown in Fig. 14. Only the subpopulations of models that resulted in spontaneous beating and normal repolarization after drug application were analyzed. Additionally, TTX response was only analyzed in the subpopulation of model cells with more than -10 pA/pF peak I_{Na} during the control (non-drug) AP. The size and results of the analyzed model subpopulations are reported in Table 4. It should be noted that the baseline model has a peak I_{Na} of -29.2 pA/pF during the AP. Models without substantial I_{Na} during the AP are unaffected by TTX, and were omitted for clarity. Highly variable iPSC-CM response to TTX and other sodium channel blockers has also been observed experimentally (Sheng *et al.*, 2012).

The drug-induced changes to AP morphology predicted by our model population falls within the experimentally observed range, as characterized in Table 4 (Peng *et al.*, 2010; Ma *et al.*, 2011; Jonsson *et al.*, 2012; Gibson *et al.*, 2014; Scheel *et al.*, 2014; Hortigon-Vinagre *et al.*, 2016). It should be noted that there is a large range of experimentally observed variation in the effects of each of these drugs. Experimental data shown in Table 4 includes data from paced and spontaneously beating cells, which may contribute to this variability. However, for TTX, Jonsson et al. shows a similar range of change in upstroke velocity in paced and spontaneously beating cells treated with TTX. Additionally, Hortigon-Vinagre et al. show that cell line differences have an impact on the observed response to Nifedpine and E-4031 in spontaneously beating APs. Hortigon-Vinargre et al. and Jonsson et al. reported AP outputs in spontaneously beating cells, while the other studies reported AP outputs at 1Hz pacing. Qualitatively, experimental results across these experimental protocols show a similar response to each ionic channel blocking drug. Our comparison of model outputs with the

experimental range reported in Table 4 serves to show that our model population can replicate this qualitative response to simple pore block.

Table 4 shows the range of the mean behavior amongst the datasets cited, but the full range of behavior in individual cells between these datasets is even larger. As discussed previously in characterizing the baseline AP morphology, it is impossible to pinpoint "normal" iPSC-CM response. There is a wide range of variability in the ionic currents regulating iPSC-CM APs, and this is reflected in the range of responses to a particular drug.

Immature and Mature Phenotypes

We next compared representative immature and mature model phenotypes. The previously described baseline model was used as the representative immature model. The representative mature model was created using the baseline model with a 100% increase in maximal conductance of I_{K1} and a 45% increase in maximal conductance of I_{Na}. These changes represent the relative increase in I_{K1} and I_{Na} from the immature to mature phenotype, as characterized experimentally by the Jalife Lab (Fig. 3B & 9). These increases in I_{K1} and I_{Na} are proportional to the increase in I_{K1} and I_{Na} peak current between iPSC-CMs cultured on glass (immature) and PDMS (mature) shown in Herron et al. (Herron *et al.*, 2016). The behavior of the immature and mature models is compared in Fig. 15. The APs of the immature and mature models are shown in Fig. 15A, and the AP morphology markers for each model are compared to experimentally measured APs from the Jalife Lab in Fig. 15B. Cell outputs (experimental and computational) were normalized to the average value of the experimental iPSC-CMs cultured on PDMS (black, Fig. 15B). Finally a multivariable regression model, created using the same methodology as described for the baseline model (Sobie, 2009) and shown in Fig. 11E, was used to conduct sensitivity analysis on both the mature and baseline/immature models, and a comparison of the results is shown in Fig.15C.

For all four AP morphology markers (MDP, AP amplitude, APD_{90}, and maximal upstroke velocity), the mature model (shown as red dots, Fig. 15B) is within the experimental range for mature cells (shown as black points in Fig. 15B). The experimental AP data, which was not utilized in fitting the mature model, serves to validate that the mature model is representative of the experimentally matured iPSC-CMs. The resulting mature model diastolic membrane potential ($MDP_{Mature,\ Model}$ = -77.4 mV) is representative of the average experimentally matured cells ($MDP_{Mature,\ Exp}$ = -77.5 mV), and has a more hyperpolarized diastolic membrane potential than the immature model ($MDP_{Immature,\ Model}$ = -75.6 mV). The AP amplitude of the mature model population is larger than the immature model population ($Amp_{Mature,Model}$ = 108 $\pm$ 6 mV, $Amp_{Immature,Model}$ = 90 $\pm$ 9 mV), which is consistent with the

experimentally observed trend of a larger AP amplitude in mature cells ($Amp_{Mature,Exp}$ = 117± 6 mV, $Amp_{Immature,Exp}$ = 105 ± 16 mV). Similarly, the APD in the mature population is slightly longer than the immature population ($APD_{90,Mature,Model}$ = 347 ± 77 ms, $APD_{90,Immature,Model}$ = 340 ± 74 ms), which is consistent with the experimental results ($APD_{90,Mature,Exp}$ = 453 ± 113 ms, $APD_{90,Immature,Exp}$ = 437 ± 173 ms). Finally, for maximal upstroke velocity (dV/dt) the mature model value ($dV/dt_{Mature,Model}$ = 199 mV/ms) is within the experimentally measured range ($dV/dt_{Mature,Exp}$ = 147 ± 87 mV/ms), and has a much higher upstroke velocity than the immature model value ($dV/dt_{Immature,Model}$ = 33 mV/ms), as would be expected in a more mature cell.

Maturation: Population-based Insights

Notably, experimentally recorded mature iPSC-CMs retained spontaneous beating while our mature model cells required stimulation to beat. This indicates that there was either an excess of I_{K1} in our representative mature model, or that other currents compensate for the increased I_{K1} allowing the mature experimental cells to retain spontaneous beating at more negative maximum diastolic potentials. This led us to analyze our population of spontaneous beating cells, to explore a computational subpopulation of cells that exhibited a mature phenotype, while retaining spontaneous beating. One of the advantages of a population-based modeling approach is the ability to utilize a component dissection approach to identify plausible ionic mechanisms of known phenotypes. As a test case, we examined the immature and mature phenotypes in our model iPSC-CM population. We formed two subpopulations of cells from the five-current variation population (Fig. 13B), based on phenotype. Based on the experimental data from the Jalife Lab, we determined ranges of cellular MDP and maximal upstroke velocity outputs which defined our immature and mature model subpopulations. The cut-off regions for MDP and upstroke velocity were determined based on the experimental outputs for matured cells (black points, Fig. 16A) compared to control cells which exhibit a more immature phenotype (open circles, Fig. 16A). We categorized mature cells as those with hyperpolarized diastolic potentials and high upstroke velocity (MDP < -75 mV, dv/dt_{max} > 85 mV/ms, red in Fig. 16A), and immature cells as those with depolarized diastolic potentials and low upstroke velocity (MDP > -75 mV, dv/dt_{max} < 85 mV/ms, blue in Fig. 16A). A third group of cellular models which did not meet either the immature or mature phenotype criteria (grey in Fig. 16A), were not analyzed.

To compare mature and immature populations, we looked at the underlying model parameters which had the largest difference between the two populations. To normalize parameter values, the population analysis was conducted using percent change in

parameter value from the baseline model parameter value, shown in Fig. 16B. The three currents identified in this analysis were I_{K1}, I_{Na}, and I_f. Maximal conductance parameters for all three currents were identified, with lower maximal conductance of I_{K1} and I_{Na} found in the immature cells, which is consistent with the findings in Herron et al. (Herron *et al.*, 2016) . Both currents are directly related to the defining characteristics of mature and immature subpopulations, as increased I_{K1} hyperpolarized the MDP and increased I_{Na} increases the maximal upstroke velocity. In addition to g_{K1} and g_{Na}, the immature population also exhibited increased g_f, which is consistent with an immature cardiomyocyte phenotype (Karakikes *et al.*, 2015; Kim *et al.*, 2015).

In additional to maximal conductances, x_6 in the formulation of I_{Na} inactivation gate was also identified. The decrease in the x_6 parameter impacts the shift in the I_{Na} inactivation (h and j) steady-state curves, as described in the methods section (Eqn. 8-9). A decrease in x_6 in the mature models corresponds to increased I_{Na} in the physiological voltage range by shifting the steady-state inactivation curve toward the physiological range, as shown for the model populations in Fig. 16C (individual models in light colors, population averages in dark colors). Similarly, x_6 shifts the negatively sloped portion of the tau decay curve, causing an increased time constant of inactivation in the relevant range for the upstroke of the AP (-70 to -50mV). An increase in time constant slows the inactivation of I_{Na}. Collectively, this change in x_6 results in more I_{Na} during the upstroke of the AP, having a combined impact with the increase in g_{Na} in mature cells, which all contribute to the increased maximal upstroke velocity. Additionally, Fig 16C shows that there are immature cells (blue, Fig. 16C) with steady-state inactivation curves resulting in V_{half} in the mature range (-85 to -50 mV), but no mature cells (pink, Fig. 16C) with V_{half}<-85 mV. This suggests that to reach a maximal upstroke velocity above 85 mV/ms, our cutoff for mature cells, the cellular I_{Na} model needs to fall within a smaller range of steady-state inactivation behaviors. This positive shift in the inactivation curve, and a corresponding increase in g_{Na} (Fig. 16B), allows for a large influx of I_{Na} during the AP upstroke, resulting in a more mature phenotype with a high upstroke velocity. Immature cells with low maximal upstroke velocity have a much wider range of steady-state inactivation curves which are compensated by a wide range of maximal I_{Na} conductance values to keep the upstroke velocity within the immature range. It should be noted that the baseline model can maintain spontaneous beating with complete I_{Na} block, as has been shown experimentally in iPSC-CMs (Guo *et al.*, 2011; Sheng *et al.*, 2012). Thus, some cells in immature population may have I_{Na} parameterizations which result in miniscule I_{Na} during spontaneous beating.

The population-based approach identified three currents (I_{Na}, I_{K1}, and I_f) which are appreciably different between the immature and mature subpopulations (Fig. 16B). Two of these currents have been experimentally validated by the Jalife Lab, as shown in Fig. 16D. Experimental measurements in matured iPSC-CMs show enhanced I_{Na} and I_{K1} compared to the control cells. The experimental and *in silico* results are shown in Fig. 16D for the mature cells. The mature cellular outputs were normalized to the respective average experimental or *in silico* immature outputs. In the model subpopulations, the peak current from the IV curve for each cell in the mature population was normalized to the mean value of the peak current in the immature population. For I_{K1} we analyzed the outward portion I_{K1}, which occurs in the physiological voltage range (V_m>85 mV) for iPSC-CMs.

While the MDP and upstroke velocity are known to be directly linked to the maximal conductance of I_{K1} and I_{Na}, respectively, this methodology also identified g_f and kinetics of I_{Na} which contribute to the mature phenotype. In the future, this approach can also be expanded to identify mechanisms of disease states. The data used to construct this model was from presumed healthy iPSC-CMs, but a similar approach could be used to identify molecular mechanisms of increased proclivity to arrhythmia or susceptibility to proarrhythmic drugs in a diseased population model.

DISCUSSION:

In this study, we present a modeling approach for *in silico* representation of iPSC-CMs. We used a “bottom-up” approach by developing models of subcellular components, namely individual ionic currents and Ca^{2+} handling proteins. This study was in collaboration with a number of experimental laboratories who generously provided data recorded from iPSC-CMs in their respective laboratories. These data allowed us to consider measured variability in ionic currents and their underlying processes. To minimize the number of model parameters, and to prevent overfitting, we utilized a simple formulation of the ionic currents with fewer parameters than other commonly used cardiomyocyte or ionic current models (ten Tusscher *et al.*, 2004; Moreno *et al.*, 2011; O'Hara *et al.*, 2011).

To gain a complete picture of the behavior of iPSC-CMs, a single average behavior is insufficient. There is no experimental consensus on which iPSC-CM recording might represent average or representative behavior. We sought to determine if variability at the subcellular level was sufficient to replicate this wide range of whole-cell iPSC-CM phenotypes. Fig. 13D-F shows that our *in silico* population, informed purely by the distribution of experimentally observed kinetic behavior, reproduces the range of whole-cell

behaviors observed experimentally. Within this population, each individual model, including the baseline model, is presumed to be an equally valid representation of an iPSC-CM.

In developing a collection of *in silico* iPSC-CMs that reflect phenotypic cellular variability, we explored populations with single current variation, as well as simultaneous variation in five key currents. While the five-current variation population provides the most complete coverage of the experimentally observed parameter space, comparing the different populations developed can provide additional insight (Fig. 13). For each of the single-current variation populations, there is a relatively narrow range of variability in whole-cell AP morphology. Additionally, nearly all models created through single current variation resulted in a viable and spontaneously beating cellular model. However, when variation in multiple currents was included in the cell representation, there was a much larger range of AP morphologies including "non-viable" *in silico* iPSC-CMs that were not possible to excite or did not repolarize.

The results described above are not surprising and may stem from physiologically relevant regulatory phenomena that require correlation and coordination of ionic currents within individual cells. For example, to have sufficient net repolarizing current during the AP, there must be a mechanism of coregulation for repolarizing currents (Xiao *et al.*, 2008; Varro & Baczko, 2011). In iPSC-CMs, and other fetal-like cell types, there is a particularly low density of I_{K1}, as compared to adult cardiomyocytes (Bett *et al.*, 2013; Meijer van Putten *et al.*, 2015; Vaidyanathan *et al.*, 2016). While our cellular populations include a large range of variation in I_{K1}, there is much lower I_{K1} density throughout these populations than there would be in an adult ventricular cardiomyocyte (Karakikes *et al.*, 2015). In particular, the lack of I_{K1} plays a key role in the spontaneously beating phenotype, which is characteristic of these cells (Kim *et al.*, 2015). Thus, there is a balance of repolarizing currents in iPSC-CMs that allow for spontaneous beating, while maintaining the cells ability to fully repolarize. As every cell in our a populations maintains spontaneous beating (Fig. 13), every cell also requires coregulation of ionic current density which maintains a unique balance of repolarizing currents to accommodate the relatively low $I_{K1.}$.

Coregulation has been shown experimentally in numerous studies of cardiac cells (Deschenes *et al.*, 2008; Xiao *et al.*, 2008; Milstein *et al.*, 2012). For example, Liu et al. showed that there is cotranslation of protein subunits, leading to functional regulation of cellular ionic currents within a single cell (Liu *et al.*, 2016). Cotranslation may also serve as a mechanism to maintain the balance of ionic currents within a single cell. Banyaz et al. showed that there is a mechanism by which individual cells regulate net ionic current,

despite a wide range of variability in density of individual currents (Banyasz *et al.*, 2011). Specifically, there was a linear relationship between the inward and outward currents measured via AP dissection, indicating a mechanism of cellular coordination between key inward and outward currents. The results of our population-based studies suggest a similar coordination in the ionic currents of iPSC-CMs, allowing for a wide range of variation in subcellular mechanisms while maintaining functional AP dynamics. Intriguingly, a recent combined computational and experimental study revealed that variable inward calcium and outward potassium currents in mouse ventricular myocytes compensate each other to generate normal calcium transients and contractile responses (Rees *et al.*, 2018). This suggests a feedback mechanism sensing global cytosolic calcium levels might be sufficient to regulate ionic conductances. Clinically, genetic modifiers have been seen to modify the severity of Long QT Syndrome type 2. Patients with the same hERG mutations have differential severity in QT prolongation, depending on the presence of other mutations which coregulate cellular repolarization (Chai *et al.*, 2018). Our study provides a framework which can be expanded to elucidate these types of feedback and coregulation mechanisms in iPSC-CMs, which directly relate to mechanisms of adult human cardiomyocyte behavior.

Sources of cellular variation are often unclear, but experimental manipulation allows us to directly compare known sources of variation. Using data from experimentally manipulated cells, we were able to validate our framework for determining sources of variation leading to known phenotypes. Using data from maturation promoted iPSC-CMs allowed us to conduct a two-pronged analysis of cell maturation. Beginning with a bottom-up approach, we showed that a single cell model can accurately predict a more mature phenotype based on known sources of variation, as shown in Fig. 15. Additionally, we used a top-down approach to test if the parameter space used to randomly generate our model populations covered the subcellular range of maturation behavior. As hypothesized, the whole-cell behavior within the population predicts a range of maturation, as shown in Fig. 16A. Additionally, our population-based approach identified the same changes in key currents (I_{Na} and I_{K1}, Fig 16D) when stratifying subpopulations of mature and immature cellular models.

This same top-down approach can be used to compare other subpopulations. We also used this approach to compare atrial and ventricular-like subpopulations. To define atrial and ventricular-like subpopulations we used a metric used experimentally to classify iPSC-CMs: $APD_r = (APD_{40} - APD_{30})/(APD_{80} - APD_{70})$(Ma *et al.*, 2011). Ventricular-like cells are defined as $APD_r > 1.5$, and atrial-like cells are $APD_r < 1.5$. Using the atrial and ventricular-like subpopulations, we conducted the same analysis shown in Fig.16B. Our analysis on the atrial and ventricular-like populations identified the maximal conductance parameters for I_{Kr}

and I_{CaL} as having the largest differences between the two subpopulations. This is consistent with experimental works by Lieu et al. in embryonic stem cell-derived cardiomyocytes (ESC-CMs), which identified the increased I_{Kr} and I_{CaL} in ventricular-like ESC-CMs, compared to atrial-like (Lieu *et al.*, 2013). They additionally showed decreased I_f in atrial-like ESC-CMs, which our analysis did not identify. The APD_r criterion was used to define the atrial and ventricular-like subpopulations in order to be consistent with the experimental methodology, and show our model captures these experimental results. However, there is debate over the precision of this definition of atrial vs. ventricular cells (Du *et al.*, 2015; Giles & Noble, 2016). This criterion considers only the AP morphology in determining the chamber specificity of the cells, which ignores many other key physiological differences between the two cell types.

The large range of experimentally observed variability in iPSC-CMs, which is recapitulated within the populations of models presented in this study, allows us to examine the mechanistic origin of phenotypic differences (Sarkar & Sobie, 2011; Yang *et al.*, 2015; Morotti & Grandi, 2017; Passini *et al.*, 2017). Properly utilized, the phenotypic variation in iPSC-CMs can be strength of this experimental approach, allowing us to better understand the mechanistic underpinnings of phenotypic diversity which is, of course, also observed in patients. iPSC-CMs in conjunction with computational approaches provide a unique opportunity to conduct high throughput component dissection of phenotypes of interest, which can ultimately be linked to patient-specific phenotypes.

Our study can also serve as a basis to “translate” the patient-specific iPSC-CM behaviors from the immature fetal-like phenotype, to a predictive model of adult cardiomyocyte behavior. As has been noted experimentally, our model population reflects the differences in AP morphology between iPSC-CMs and adult ventricular cells. On average, our model population has a more positive resting membrane potential, slower AP upstroke velocity, slower CaT time to peak, and reduced CaT amplitude comparted to adult ventricular cell models (ten Tusscher *et al.*, 2004; O'Hara *et al.*, 2011). Understanding the mechanisms of these differences is the first step to translating between iPSC-CM and adult cardiac response. Critical differences between ionic currents in adult and iPSC-CM have been noted in computational and experimental studies (Karakikes *et al.*, 2015; Paci *et al.*, 2015). Translation between iPSC-CM and adult phenotypes will be critical in the use of iPSC-CMs for drug safety and discovery in the human population. Gong and Sobie have developed a cross-cell type regression model that translates response to ionic current perturbations in an iPSC-CM model to the predicted the response in an adult ventricular cardiomyocyte model (Gong & Sobie, 2018). Additionally, Tvieto et al. have developed a method of utilizing optically obtained experimental whole-cell drug-response data from immature iPSC-CMs to

computationally predict the effect in a mature iPSC-CM phenotype, which serves as a more representative model of adult cardiomyocytes (Tveito *et al.*, 2018). In the future, these computational translation approaches can be coupled with our utilization of experimental data from multiple sources to further reconcile the phenotypic variability observed across iPSC-CM datasets with patient-specific adult cardiac phenotypes.

LIMITATIONS:

In part, the goal of this modeling approach was to fully parameterize a model from experimental data with the fewest parameters possible, and still recapitulate complex behavior which has been characterized in iPSC-CMs. However, it should be noted that there is no complete experimental characterization of calcium handling, sodium handling, or E-C coupling in iPSC-CMs. This a critical point of concern with the adaptation of iPSC-CMs in the study of drug and disease mechanisms. Furthermore, pumps and exchangers also lack experimental characterization in iPSC-CMs. We have modeled the iPSC-CM calcium handling based on all available experimental data, resulting in more experimentally-based iPSC-CM calcium handling than prior modeling efforts. Our model captures the physiological reality for SR-calcium release dependence on cytosolic concentration, faithfully reproduces the experimentally measured contribution of various calcium removal processes, and utilizes experimentally-based calcium buffering parameters. Moreover, we are confident in the validity of adopting earlier model formulations of pumps and exchangers as these mechanisms maintain intrinsic transport stoichiometry and kinetics across various cells. Nonetheless, the implementation of phenomena which are not fully experimentally characterized in iPSC-CMs remains a limitation of our model.

Additionally, an essential gap in knowledge remains related to the source of observed experimental variation. As some of this variation may come from the cell-culture process or the cell-type, in future work it would be beneficial to collect a full kinetic characterization of individual cells. A necessary next step is to fully parameterize a cellular model based on the kinetics of individual cells. This future goal will be required to utilize iPSC-CMs for the pursuit of patient-specific models.

CONCLUSIONS:

We have utilized multiple iPSC-CM ion channel data sources to construct a range of ion channel models for key iPSC-CM currents. We then utilized random selection of parameters from within the model ranges to inform development of a population of cellular level iPSC-CM models. Several conclusions can be drawn: 1) Variation in the underlying model

parameters within the experimentally measured ranges were sufficient to encapsulate the complete diverse range of whole-cell iPSC-CM phenotypes that are observed experimentally. 2) This method to derive a population of model cells obviated the need for "calibration" or selecting models that exhibit physiologically relevant electrical behavior, beyond excluding non-excitable or non-repolarizing cells. 3) Mature and immature iPSC-CM phenotypes naturally emerge as subsets of the population.

The construction presented here has many potential future applications which can aid in understanding cardiac disease and drug testing. In conjunction with the existing CiPA protocol (Cavero & Holzgrefe, 2014), the iPSC-CM computational model here can be applied to provide a better understanding of parameter combinations which lead to proarrhythmic behaviors. This *in silico* population-based framework for analyzing iPSC-CM phenotype has the added advantage of being a high throughput analysis tool. Additionally, the models that we present can be readily expanded to include genetic mutations, pharmacological interventions, sex-based differences, and a variety of perturbations. Future studies could utilize coupled sheets of *in silico* tissue to test higher dimension arrhythmia proclivity and sustainability.

ADDITIONAL INFORMATION:

Competing Interests:

None of the authors have any conflicts of interests.

Author Contributions:

D.C.K. designed and performed simulations, analyzed data, and prepared the manuscript; S.M. designed and performed simulations, analyzed data, and revised the manuscript. H.W., P.G., H.J.D., J.K., J.J., and J.C.W. designed and performed experiments, and revised the manuscript; E.G. and C.E.C. designed simulations and experiments, analyzed data, coordinated and oversaw the project, and prepared the manuscript. All authors have approved the final version of the manuscript and agree to be accountable for all aspects of the work. All persons designated as authors qualify for authorship, and all those who qualify for authorship are listed.

Funding:

National Institutes of Health NHLBI U01HL126273, R01HL128537, R01HL128170 (to C.E.C.). The National Institutes of Health Common Fund OT2OD026580 (to C.E.C. and E.G.). American Heart Association grant 15SDG24910015, National Institutes of Health NHLBI R01HL131517, R01HL41214, UC Davis School of Medicine Dean's Fellow award (to E.G.). National Institutes of Health NHLBI R24HL117756, R01HL113006 (to J.C.W.). National Institutes of Health NHLBI R01HL122352, Grants from Transatlantic Networks of Excellence Program from the Leducq Foundation, and Fondos FEDER, Madrid, Spain (to J.J.). NHLBI K99HL138160 award (to S.M.). Predoctoral Fellowship from NIH NHLBI Institutional Training Grant T32HL086350 (to D.C.K.).

Translational Perspective:

Induced pluripotent stem cell-derived cardiomyocytes (iPSC-CMs) have been developed as a promising *in vitro* method to address patient-specific proclivity to cardiac disease and drug response. A well-known limitation of iPSC-CMs is the cell-to-cell variability observed in electrical activity. We hypothesize that when captured in a computational framework, cell-to-cell variability may constitute a useful systems property that can allow for identification of a variety of phenotypic mechanisms and underlying causal components. We have developed a whole-cell model of iPSC-CMs composed of simple model components built on experimental data from multiple laboratories. By including a wide range of input data into the model, we built a population of cellular models that predict robust inter-subject variability in iPSC-CMs. This approach allows for link between molecular mechanisms and emergent cellular-level iPSC-CM phenotypes to be revealed. The mechanisms underlying immature and mature subpopulations are predicted and consistent with experimental data. In the future, the models presented may prove essential to integrate experimental and clinical data from a variety of sources, scales, and modalities to allow high throughput prediction of the link between patient phenotype and patient specific electrophysiology. Tools presented here can be readily expanded and applied for *in silico* screening and prediction of drug effects on varied genetic backgrounds to predict patient pharmacological responses and even to guide *therapy* for specific patient therapy.

REFERENCES:

Banyasz T, Horvath B, Jian Z, Izu LT & Chen-Izu Y. (2011). Sequential dissection of multiple ionic currents in single cardiac myocytes under action potential-clamp. *J Mol Cell Cardiol* **50,** 578-581.

Beeler GW & Reuter H. (1977). Reconstruction of the action potential of ventricular myocardial fibres. *J Physiol* **268,** 177-210.

Behr ER & Roden D. (2013). Drug-induced arrhythmia: pharmacogenomic prescribing? *Eur Heart J* **34,** 89-95.

Bellin M, Casini S, Davis RP, D'Aniello C, Haas J, Ward-van Oostwaard D, Tertoolen LG, Jung CB, Elliott DA, Welling A, Laugwitz KL, Moretti A & Mummery CL. (2013). Isogenic human pluripotent stem cell pairs reveal the role of a KCNH2 mutation in long-QT syndrome. *EMBO J* **32,** 3161-3175.

Bers DM. (2000). Calcium fluxes involved in control of cardiac myocyte contraction. *Circ Res* **87,** 275-281.

Bett GC, Kaplan AD, Lis A, Cimato TR, Tzanakakis ES, Zhou Q, Morales MJ & Rasmusson RL. (2013). Electronic "expression" of the inward rectifier in cardiocytes derived from human-induced pluripotent stem cells. *Heart Rhythm* **10,** 1903-1910.

Britton OJ, Bueno-Orovio A, Van Ammel K, Lu HR, Towart R, Gallacher DJ & Rodriguez B. (2013). Experimentally calibrated population of models predicts and explains intersubject variability in cardiac cellular electrophysiology. *Proc Natl Acad Sci U S A* **110,** E2098-2105.

Burridge PW, Li YF, Matsa E, Wu H, Ong SG, Sharma A, Holmstrom A, Chang AC, Coronado MJ, Ebert AD, Knowles JW, Telli ML, Witteles RM, Blau HM, Bernstein D, Altman RB & Wu JC. (2016). Human induced pluripotent stem cell-derived cardiomyocytes recapitulate the predilection of breast cancer patients to doxorubicin-induced cardiotoxicity. *Nat Med* **22,** 547-556.

Cavero I & Holzgrefe H. (2014). Comprehensive in vitro Proarrhythmia Assay, a novel in vitro/in silico paradigm to detect ventricular proarrhythmic liability: a visionary 21st century initiative. *Expert Opin Drug Saf* **13,** 745-758.

Chai S, Wan X, Ramirez-Navarro A, Tesar PJ, Kaufman ES, Ficker E, George AL, Jr. & Deschenes I. (2018). Physiological genomics identifies genetic modifiers of long QT syndrome type 2 severity. *J Clin Invest* **128,** 1043-1056.

Cordeiro JM, Nesterenko VV, Sicouri S, Goodrow RJ, Jr., Treat JA, Desai M, Wu Y, Doss MX, Antzelevitch C & Di Diego JM. (2013). Identification and characterization of a transient outward K+ current in human induced pluripotent stem cell-derived cardiomyocytes. *J Mol Cell Cardiol* **60,** 36-46.

Correa AM, Latorre R & Bezanilla F. (1991). Ion permeation in normal and batrachotoxin-modified Na+ channels in the squid giant axon. *J Gen Physiol* **97,** 605-625.

DeBoever C, Li H, Jakubosky D, Benaglio P, Reyna J, Olson KM, Huang H, Biggs W, Sandoval E, D'Antonio M, Jepsen K, Matsui H, Arias A, Ren B, Nariai N, Smith EN, D'Antonio-Chronowska A, Farley EK & Frazer KA. (2017). Large-Scale Profiling Reveals the Influence of Genetic Variation on Gene Expression in Human Induced Pluripotent Stem Cells. *Cell Stem Cell* **20,** 533-546 e537.

Deschenes I, Armoundas AA, Jones SP & Tomaselli GF. (2008). Post-transcriptional gene silencing of KChIP2 and Navbeta1 in neonatal rat cardiac myocytes reveals a functional association between Na and Ito currents. *J Mol Cell Cardiol* **45,** 336-346.

DiFrancesco D & Noble D. (1985). A model of cardiac electrical activity incorporating ionic pumps and concentration changes. *Philos Trans R Soc Lond B Biol Sci* **307,** 353-398.

Doss MX, Di Diego JM, Goodrow RJ, Wu Y, Cordeiro JM, Nesterenko VV, Barajas-Martinez H, Hu D, Urrutia J, Desai M, Treat JA, Sachinidis A & Antzelevitch C. (2012). Maximum diastolic potential of human induced pluripotent stem cell-derived cardiomyocytes depends critically on I(Kr). *PLoS One* **7,** e40288.

Du DTM, Hellen N, Kane C & Terracciano CMN. (2015). Action Potential Morphology of Human Induced Pluripotent Stem Cell-Derived Cardiomyocytes Does Not Predict Cardiac Chamber Specificity and Is Dependent on Cell Density. *Biophysical Journal* **108,** 1-4.

Es-Salah-Lamoureux Z, Jouni M, Malak OA, Belbachir N, Al Sayed ZR, Gandon-Renard M, Lamirault G, Gauthier C, Baro I, Charpentier F, Zibara K, Lemarchand P, Beaumelle B, Gaborit N & Loussouarn G. (2016). HIV-Tat induces a decrease in IKr and IKsvia reduction in phosphatidylinositol-(4,5)-bisphosphate availability. *J Mol Cell Cardiol* **99,** 1-13.

Fermini B, Hancox JC, Abi-Gerges N, Bridgland-Taylor M, Chaudhary KW, Colatsky T, Correll K, Crumb W, Damiano B, Erdemli G, Gintant G, Imredy J, Koerner J, Kramer J, Levesque P, Li Z, Lindqvist A, Obejero-Paz CA, Rampe D, Sawada K, Strauss DG & Vandenberg JI. (2015). A New Perspective in the Field of Cardiac Safety Testing through the Comprehensive In Vitro Proarrhythmia Assay Paradigm. *J Biomol Screen*.

Garg P, Oikonomopoulos A, Chen H, Li Y, Lam CK, Sallam K, Perez M, Lux RL, Sanguinetti MC & Wu JC. (2018). Genome Editing of Induced Pluripotent Stem Cells to Decipher Cardiac Channelopathy Variant. *J Am Coll Cardiol* **72,** 62-75.

Gibson JK, Yue Y, Bronson J, Palmer C & Numann R. (2014). Human stem cell-derived cardiomyocytes detect drug-mediated changes in action potentials and ion currents. *J Pharmacol Toxicol Methods* **70,** 255-267.

Giles WR & Noble D. (2016). Rigorous Phenotyping of Cardiac iPSC Preparations Requires Knowledge of Their Resting Potential(s). *Biophys J* **110,** 278-280.

Gong JQX & Sobie EA. (2018). Population-based mechanistic modeling allows for quantitative predictions of drug responses across cell types. *NPJ Syst Biol Appl* **4,** 11.

Guo L, Abrams RM, Babiarz JE, Cohen JD, Kameoka S, Sanders MJ, Chiao E & Kolaja KL. (2011). Estimating the risk of drug-induced proarrhythmia using human induced pluripotent stem cell-derived cardiomyocytes. *Toxicol Sci* **123,** 281-289.

Harris K, Aylott M, Cui Y, Louttit JB, McMahon NC & Sridhar A. (2013). Comparison of electrophysiological data from human-induced pluripotent stem cell-derived cardiomyocytes to functional preclinical safety assays. *Toxicol Sci* **134,** 412-426.

Herron TJ, Rocha AM, Campbell KF, Ponce-Balbuena D, Willis BC, Guerrero-Serna G, Liu Q, Klos M, Musa H, Zarzoso M, Bizy A, Furness J, Anumonwo J, Mironov S & Jalife J. (2016). Extracellular Matrix-Mediated Maturation of Human Pluripotent Stem Cell-Derived Cardiac Monolayer Structure and Electrophysiological Function. *Circ Arrhythm Electrophysiol* **9,** e003638.

Hodgkin AL & Huxley AF. (1952). A quantitative description of membrane current and its application to conduction and excitation in nerve. *J Physiol* **117,** 500-544.

Hortigon-Vinagre MP, Zamora V, Burton FL, Green J, Gintant GA & Smith GL. (2016). The Use of Ratiometric Fluorescence Measurements of the Voltage Sensitive Dye Di-4-ANEPPS to Examine Action Potential Characteristics and Drug Effects on Human Induced Pluripotent Stem Cell-Derived Cardiomyocytes. *Toxicol Sci* **154,** 320-331.

Hwang HS, Kryshtal DO, Feaster TK, Sanchez-Freire V, Zhang J, Kamp TJ, Hong CC, Wu JC & Knollmann BC. (2015). Comparable calcium handling of human iPSC-derived cardiomyocytes generated by multiple laboratories. *J Mol Cell Cardiol* **85,** 79-88.

Itzhaki I, Maizels L, Huber I, Zwi-Dantsis L, Caspi O, Winterstern A, Feldman O, Gepstein A, Arbel G, Hammerman H, Boulos M & Gepstein L. (2011). Modelling the long QT syndrome with induced pluripotent stem cells. *Nature* **471,** 225-229.

Ivashchenko CY, Pipes GC, Lozinskaya IM, Lin Z, Xiaoping X, Needle S, Grygielko ET, Hu E, Toomey JR, Lepore JJ & Willette RN. (2013). Human-induced pluripotent stem cell-derived cardiomyocytes exhibit temporal changes in phenotype. *American journal of physiology Heart and circulatory physiology* **305,** H913-922.

Jamshidi Y, Nolte IM, Dalageorgou C, Zheng D, Johnson T, Bastiaenen R, Ruddy S, Talbott D, Norris KJ, Snieder H, George AL, Marshall V, Shakir S, Kannankeril PJ, Munroe PB, Camm AJ, Jeffery S, Roden DM & Behr ER. (2012). Common variation in the NOS1AP gene is associated with drug-induced QT prolongation and ventricular arrhythmia. *J Am Coll Cardiol* **60,** 841-850.

Jonsson MK, Vos MA, Mirams GR, Duker G, Sartipy P, de Boer TP & van Veen TA. (2012). Application of human stem cell-derived cardiomyocytes in safety pharmacology requires caution beyond hERG. *J Mol Cell Cardiol* **52,** 998-1008.

Kaab S, Crawford DC, Sinner MF, Behr ER, Kannankeril PJ, Wilde AA, Bezzina CR, Schulze-Bahr E, Guicheney P, Bishopric NH, Myerburg RJ, Schott JJ, Pfeufer A, Beckmann BM, Martens E, Zhang T, Stallmeyer B, Zumhagen S, Denjoy I, Bardai A, Van Gelder IC, Jamshidi Y, Dalageorgou C, Marshall V, Jeffery S, Shakir S, Camm AJ, Steinbeck G, Perz S, Lichtner P, Meitinger T, Peters A, Wichmann HE, Ingram C, Bradford Y, Carter S, Norris K, Ritchie MD, George AL, Jr. & Roden DM. (2012). A large candidate gene survey identifies the KCNE1 D85N polymorphism as a possible modulator of drug-induced torsades de pointes. *Circulation Cardiovascular genetics* **5,** 91-99.

Kamakura T, Makiyama T, Sasaki K, Yoshida Y, Wuriyanghai Y, Chen J, Hattori T, Ohno S, Kita T, Horie M, Yamanaka S & Kimura T. (2013). Ultrastructural maturation of human-induced pluripotent stem cell-derived cardiomyocytes in a long-term culture. *Circ J* **77,** 1307-1314.

Karakikes I, Ameen M, Termglinchan V & Wu JC. (2015). Human induced pluripotent stem cell-derived cardiomyocytes: insights into molecular, cellular, and functional phenotypes. *Circulation research* **117,** 80-88.

Karakikes I, Termglinchan V & Wu JC. (2014). Human-induced pluripotent stem cell models of inherited cardiomyopathies. *Curr Opin Cardiol* **29,** 214-219.

Kim JJ, Yang L, Lin B, Zhu X, Sun B, Kaplan AD, Bett GC, Rasmusson RL, London B & Salama G. (2015). Mechanism of automaticity in cardiomyocytes derived from human induced pluripotent stem cells. *J Mol Cell Cardiol* **81,** 81-93.

Kiyosue T, Arita M, Muramatsu H, Spindler AJ & Noble D. (1993). Ionic mechanisms of action potential prolongation at low temperature in guinea-pig ventricular myocytes. *J Physiol* **468,** 85-106.

Koivumaki JT, Naumenko N, Tuomainen T, Takalo J, Oksanen M, Puttonen KA, Lehtonen S, Kuusisto J, Laakso M, Koistinaho J & Tavi P. (2018). Structural Immaturity of Human iPSC-Derived Cardiomyocytes: In Silico Investigation of Effects on Function and Disease Modeling. *Front Physiol* **9,** 80.

Kurokawa J, Motoike HK & Kass RS. (2001). TEA(+)-sensitive KCNQ1 constructs reveal pore-independent access to KCNE1 in assembled I(Ks) channels. *J Gen Physiol* **117,** 43-52.

Lan F, Lee AS, Liang P, Sanchez-Freire V, Nguyen PK, Wang L, Han L, Yen M, Wang Y, Sun N, Abilez OJ, Hu S, Ebert AD, Navarrete EG, Simmons CS, Wheeler M, Pruitt B, Lewis R, Yamaguchi Y, Ashley EA, Bers DM, Robbins RC, Longaker MT & Wu JC. (2013). Abnormal calcium handling properties underlie familial hypertrophic cardiomyopathy pathology in patient-specific induced pluripotent stem cells. *Cell Stem Cell* **12,** 101-113.

Lei CL, Wang K, Clerx M, Johnstone RH, Hortigon-Vinagre MP, Zamora V, Allan A, Smith GL, Gavaghan DJ, Mirams GR & Polonchuk L. (2017). Tailoring Mathematical Models to Stem-Cell Derived Cardiomyocyte Lines Can Improve Predictions of Drug-Induced Changes to Their Electrophysiology. *Front Physiol* **8,** 986.

Leopold JA & Loscalzo J. (2018). Emerging Role of Precision Medicine in Cardiovascular Disease. *Circ Res* **122,** 1302-1315.

Li M, Kanda Y, Ashihara T, Sasano T, Nakai Y, Kodama M, Hayashi E, Sekino Y, Furukawa T & Kurokawa J. (2017). Overexpression of KCNJ2 in induced pluripotent stem cell-derived cardiomyocytes for the assessment of QT-prolonging drugs. *J Pharmacol Sci* **134,** 75-85.

Liang P, Lan F, Lee AS, Gong T, Sanchez-Freire V, Wang Y, Diecke S, Sallam K, Knowles JW, Wang PJ, Nguyen PK, Bers DM, Robbins RC & Wu JC. (2013). Drug screening using a library of human induced pluripotent stem cell-derived cardiomyocytes reveals disease-specific patterns of cardiotoxicity. *Circulation* **127,** 1677-1691.

Lieu DK, Fu JD, Chiamvimonvat N, Tung KC, McNerney GP, Huser T, Keller G, Kong CW & Li RA. (2013). Mechanism-based facilitated maturation of human pluripotent stem cell-derived cardiomyocytes. *Circ Arrhythm Electrophysiol* **6,** 191-201.

Liu F, Jones DK, de Lange WJ & Robertson GA. (2016). Cotranslational association of mRNA encoding subunits of heteromeric ion channels. *P Natl Acad Sci USA* **113,** 4859-4864.

Luo CH & Rudy Y. (1994). A dynamic model of the cardiac ventricular action potential. I. Simulations of ionic currents and concentration changes. *Circ Res* **74,** 1071-1096.

Ma D, Wei H, Lu J, Huang D, Liu Z, Loh LJ, Islam O, Liew R, Shim W & Cook SA. (2015). Characterization of a novel KCNQ1 mutation for type 1 long QT syndrome and assessment of the therapeutic potential of a novel IKs activator using patient-specific induced pluripotent stem cell-derived cardiomyocytes. *Stem Cell Res Ther* **6,** 39.

Ma J, Guo L, Fiene SJ, Anson BD, Thomson JA, Kamp TJ, Kolaja KL, Swanson BJ & January CT. (2011). High purity human-induced pluripotent stem cell-derived cardiomyocytes: electrophysiological properties of action potentials and ionic currents. *Am J Physiol Heart Circ Physiol* **301,** H2006-2017.

Maltsev VA & Lakatta EG. (2009). Synergism of coupled subsarcolemmal Ca2+ clocks and sarcolemmal voltage clocks confers robust and flexible pacemaker function in a novel pacemaker cell model. *Am J Physiol Heart Circ Physiol* **296,** H594-615.

Meijer van Putten RM, Mengarelli I, Guan K, Zegers JG, van Ginneken AC, Verkerk AO & Wilders R. (2015). Ion channelopathies in human induced pluripotent stem cell derived cardiomyocytes: a dynamic clamp study with virtual IK1. *Front Physiol* **6,** 7.

Milstein ML, Musa H, Balbuena DP, Anumonwo JM, Auerbach DS, Furspan PB, Hou L, Hu B, Schumacher SM, Vaidyanathan R, Martens JR & Jalife J. (2012). Dynamic reciprocity of sodium and potassium channel expression in a macromolecular complex controls cardiac excitability and arrhythmia. *Proc Natl Acad Sci U S A* **109,** E2134-2143.

Moreau A, Mercier A, Theriault O, Boutjdir M, Burger B, Keller DI & Chahine M. (2017). Biophysical, Molecular, and Pharmacological Characterization of Voltage-Dependent Sodium Channels From Induced Pluripotent Stem Cell-Derived Cardiomyocytes. *Can J Cardiol* **33,** 269-278.

Moreno JD, Lewis TJ & Clancy CE. (2016). Parameterization for In-Silico Modeling of Ion Channel Interactions with Drugs. *PLoS One* **11,** e0150761.

Moreno JD, Zhu ZI, Yang PC, Bankston JR, Jeng MT, Kang C, Wang L, Bayer JD, Christini DJ, Trayanova NA, Ripplinger CM, Kass RS & Clancy CE. (2011). A computational model to predict the effects of class I anti-arrhythmic drugs on ventricular rhythms. *Sci Transl Med* **3,** 98ra83.

Moretti A, Bellin M, Welling A, Jung CB, Lam JT, Bott-Flugel L, Dorn T, Goedel A, Hohnke C, Hofmann F, Seyfarth M, Sinnecker D, Schomig A & Laugwitz KL. (2010). Patient-specific induced pluripotent stem-cell models for long-QT syndrome. *N Engl J Med* **363,** 1397-1409.

Morotti S & Grandi E. (2017). Logistic regression analysis of populations of electrophysiological models to assess proarrythmic risk. *MethodsX* **4,** 25-34.

Muszkiewicz A, Britton OJ, Gemmell P, Passini E, Sanchez C, Zhou X, Carusi A, Quinn TA, Burrage K, Bueno-Orovio A & Rodriguez B. (2016). Variability in cardiac electrophysiology: Using experimentally-calibrated populations of models to move beyond the single virtual physiological human paradigm. *Prog Biophys Mol Biol* **120,** 115-127.

Narsinh KH, Sun N, Sanchez-Freire V, Lee AS, Almeida P, Hu S, Jan T, Wilson KD, Leong D, Rosenberg J, Yao M, Robbins RC & Wu JC. (2011). Single cell transcriptional profiling reveals heterogeneity of human induced pluripotent stem cells. *J Clin Invest* **121,** 1217-1221.

Navarrete EG, Liang P, Lan F, Sanchez-Freire V, Simmons C, Gong T, Sharma A, Burridge PW, Patlolla B, Lee AS, Wu H, Beygui RE, Wu SM, Robbins RC, Bers DM & Wu JC. (2013). Screening drug-induced arrhythmia [corrected] using human induced pluripotent stem cell-derived cardiomyocytes and low-impedance microelectrode arrays. *Circulation* **128,** S3-13.

Ni H, Morotti S & Grandi E. (2018). A Heart for Diversity: Simulating Variability in Cardiac Arrhythmia Research. *Front Physiol* **9,** 958.

Nunes SS, Miklas JW, Liu J, Aschar-Sobbi R, Xiao Y, Zhang B, Jiang J, Masse S, Gagliardi M, Hsieh A, Thavandiran N, Laflamme MA, Nanthakumar K, Gross GJ, Backx PH, Keller G & Radisic M. (2013). Biowire: a platform for maturation of human pluripotent stem cell-derived cardiomyocytes. *Nat Methods* **10,** 781-787.

O'Hara T, Virag L, Varro A & Rudy Y. (2011). Simulation of the undiseased human cardiac ventricular action potential: model formulation and experimental validation. *PLoS Comput Biol* **7,** e1002061.

Ono K & Iijima T. (2010). Cardiac T-type Ca(2+) channels in the heart. *J Mol Cell Cardiol* **48,** 65-70.

Paci M, Casini S, Bellin M, Hyttinen J & Severi S. (2018). Large-Scale Simulation of the Phenotypical Variability Induced by Loss-of-Function Long QT Mutations in Human Induced Pluripotent Stem Cell Cardiomyocytes. *Int J Mol Sci* **19**.

Paci M, Hyttinen J, Aalto-Setala K & Severi S. (2013). Computational models of ventricular- and atrial-like human induced pluripotent stem cell derived cardiomyocytes. *Ann Biomed Eng* **41,** 2334-2348.

Paci M, Hyttinen J, Rodriguez B & Severi S. (2015). Human induced pluripotent stem cell-derived versus adult cardiomyocytes: an in silico electrophysiological study on effects of ionic current block. *Br J Pharmacol* **172,** 5147-5160.

Paci M, Passini E, Severi S, Hyttinen J & Rodriguez B. (2017). Phenotypic variability in LQT3 human induced pluripotent stem cell-derived cardiomyocytes and their response to antiarrhythmic pharmacologic therapy: An in silico approach. *Heart Rhythm* **14,** 1704-1712.

Paci M, Sartiani L, Del Lungo M, Jaconi M, Mugelli A, Cerbai E & Severi S. (2012). Mathematical modelling of the action potential of human embryonic stem cell derived cardiomyocytes. *Biomed Eng Online* **11,** 61.

Passini E, Britton OJ, Lu HR, Rohrbacher J, Hermans AN, Gallacher DJ, Greig RJH, Bueno-Orovio A & Rodriguez B. (2017). Human In Silico Drug Trials Demonstrate Higher Accuracy than Animal Models in Predicting Clinical Pro-Arrhythmic Cardiotoxicity. *Front Physiol* **8,** 668.

Peng S, Lacerda AE, Kirsch GE, Brown AM & Bruening-Wright A. (2010). The action potential and comparative pharmacology of stem cell-derived human cardiomyocytes. *J Pharmacol Toxicol Methods* **61,** 277-286.

Rees CM, Yang JH, Santolini M, Lusis AJ, Weiss JN & Karma A. (2018). The Ca(2+) transient as a feedback sensor controlling cardiomyocyte ionic conductances in mouse populations. *Elife* **7**.

Rudy Y & Silva JR. (2006). Computational biology in the study of cardiac ion channels and cell electrophysiology. *Q Rev Biophys* **39,** 57-116.

Sallam K, Li Y, Sager PT, Houser SR & Wu JC. (2015). Finding the rhythm of sudden cardiac death: new opportunities using induced pluripotent stem cell-derived cardiomyocytes. *Circ Res* **116,** 1989-2004.

Sarkar AX & Sobie EA. (2010). Regression analysis for constraining free parameters in electrophysiological models of cardiac cells. *PLoS Comput Biol* **6,** e1000914.

Sarkar AX & Sobie EA. (2011). Quantification of repolarization reserve to understand interpatient variability in the response to proarrhythmic drugs: a computational analysis. *Heart Rhythm* **8,** 1749-1755.

Scheel O, Frech S, Amuzescu B, Eisfeld J, Lin KH & Knott T. (2014). Action potential characterization of human induced pluripotent stem cell-derived cardiomyocytes using automated patch-clamp technology. *Assay Drug Dev Technol* **12,** 457-469.

Schwartz PJ, Priori SG, Locati EH, Napolitano C, Cantu F, Towbin JA, Keating MT, Hammoude H, Brown AM, Chen LS & Colatsky TJ. (1995). Long QT syndrome patients with mutations of the SCN5A and HERG genes have differential responses to Na+ channel blockade and to increases in heart rate. Implications for gene-specific therapy. *Circulation* **92,** 3381-3386.

Schwartz PJ, Priori SG, Spazzolini C, Moss AJ, Vincent GM, Napolitano C, Denjoy I, Guicheney P, Breithardt G, Keating MT, Towbin JA, Beggs AH, Brink P, Wilde AA, Toivonen L, Zareba W, Robinson JL, Timothy KW, Corfield V, Wattanasirichaigoon D, Corbett C, Haverkamp W, Schulze-Bahr E, Lehmann MH, Schwartz K, Coumel P & Bloise R. (2001). Genotype-phenotype correlation in the long-QT syndrome: gene-specific triggers for life-threatening arrhythmias. *Circulation* **103,** 89-95.

Shah M & Carter C. (2008). Long QT syndrome: A therapeutic challenge. *Ann Pediatr Cardiol* **1,** 18-26.

Shannon TR, Wang F, Puglisi J, Weber C & Bers DM. (2004). A mathematical treatment of integrated Ca dynamics within the ventricular myocyte. *Biophys J* **87,** 3351-3371.

Sheng X, Reppel M, Nguemo F, Mohammad FI, Kuzmenkin A, Hescheler J & Pfannkuche K. (2012). Human pluripotent stem cell-derived cardiomyocytes: response to TTX and lidocain reveals strong cell to cell variability. *PLoS One* **7,** e45963.

Sobie EA. (2009). Parameter sensitivity analysis in electrophysiological models using multivariable regression. *Biophys J* **96,** 1264-1274.

Sun N, Yazawa M, Liu J, Han L, Sanchez-Freire V, Abilez OJ, Navarrete EG, Hu S, Wang L, Lee A, Pavlovic A, Lin S, Chen R, Hajjar RJ, Snyder MP, Dolmetsch RE, Butte MJ, Ashley EA, Longaker MT, Robbins RC & Wu JC. (2012). Patient-specific induced pluripotent stem cells as a model for familial dilated cardiomyopathy. *Sci Transl Med* **4,** 130ra147.

Takahashi K & Yamanaka S. (2006). Induction of pluripotent stem cells from mouse embryonic and adult fibroblast cultures by defined factors. *Cell* **126,** 663-676.

ten Tusscher KH, Noble D, Noble PJ & Panfilov AV. (2004). A model for human ventricular tissue. *Am J Physiol Heart Circ Physiol* **286,** H1573-1589.

Terrenoire C, Wang K, Tung KW, Chung WK, Pass RH, Lu JT, Jean JC, Omari A, Sampson KJ, Kotton DN, Keller G & Kass RS. (2013). Induced pluripotent stem cells used to reveal drug actions in a long QT syndrome family with complex genetics. *J Gen Physiol* **141,** 61-72.

Tiburcy M, Hudson JE, Balfanz P, Schlick S, Meyer T, Chang Liao ML, Levent E, Raad F, Zeidler S, Wingender E, Riegler J, Wang M, Gold JD, Kehat I, Wettwer E, Ravens U, Dierickx P, van Laake LW, Goumans MJ, Khadjeh S, Toischer K, Hasenfuss G, Couture LA, Unger A, Linke WA, Araki T, Neel B, Keller G, Gepstein L, Wu JC & Zimmermann WH. (2017). Defined Engineered Human Myocardium With Advanced Maturation for Applications in Heart Failure Modeling and Repair. *Circulation* **135,** 1832-1847.

Tveito A, Jaeger KH, Huebsch N, Charrez B, Edwards AG, Wall S & Healy KE. (2018). Inversion and computational maturation of drug response using human stem cell derived cardiomyocytes in microphysiological systems. *Sci Rep* **8,** 17626.

Vaidyanathan R, Markandeya YS, Kamp TJ, Makielski JC, January CT & Eckhardt LL. (2016). IK1-enhanced human-induced pluripotent stem cell-derived cardiomyocytes: an improved cardiomyocyte model to investigate inherited arrhythmia syndromes. *Am J Physiol Heart Circ Physiol* **310,** H1611-1621.

Varro A & Baczko I. (2011). Cardiac ventricular repolarization reserve: a principle for understanding drug-related proarrhythmic risk. *Br J Pharmacol* **164,** 14-36.

Vassort G, Talavera K & Alvarez JL. (2006). Role of T-type Ca2+ channels in the heart. *Cell Calcium* **40,** 205-220.

Veerman CC, Mengarelli I, Guan K, Stauske M, Barc J, Tan HL, Wilde AA, Verkerk AO & Bezzina CR. (2016). hiPSC-derived cardiomyocytes from Brugada Syndrome patients without identified mutations do not exhibit clear cellular electrophysiological abnormalities. *Sci Rep* **6,** 30967.

Verkerk AO & Wilders R. (2013). Hyperpolarization-activated current, If, in mathematical models of rabbit sinoatrial node pacemaker cells. *Biomed Res Int* **2013,** 872454.

Xiao L, Xiao J, Luo X, Lin H, Wang Z & Nattel S. (2008). Feedback remodeling of cardiac potassium current expression: a novel potential mechanism for control of repolarization reserve. *Circulation* **118,** 983-992.

Yang PC & Clancy CE. (2012). In silico Prediction of Sex-Based Differences in Human Susceptibility to Cardiac Ventricular Tachyarrhythmias. *Front Physiol* **3,** 360.

Yang PC, El-Bizri N, Romero L, Giles WR, Rajamani S, Belardinelli L & Clancy CE. (2016). A computational model predicts adjunctive pharmacotherapy for cardiac safety via selective inhibition of the late cardiac Na current. *J Mol Cell Cardiol* **99,** 151-161.

Yang PC, Song Y, Giles WR, Horvath B, Chen-Izu Y, Belardinelli L, Rajamani S & Clancy CE. (2015). A computational modelling approach combined with cellular electrophysiology data provides insights into the therapeutic benefit of targeting the late Na+ current. *J Physiol* **593,** 1429-1442.

Yang X, Pabon L & Murry CE. (2014). Engineering adolescence: maturation of human pluripotent stem cell-derived cardiomyocytes. *Circ Res* **114,** 511-523.

Table 1:

					Extracellular (mM)				Intracellular (mM)					
	Reference:	Temp	n=	cell-line	NaCl	KCl	CaCl2	NMDG	KCl	K-Gluconn.	K-Aspar.	NaCl	CaCl2	Na2-ATP
Ina	Ma et al. (2011)	35-37	5	iCell	50		1.8					10	2	
	Herron et al. (PDMS/ glass)	21-22	19/12	iCell	20		1.8					5		
	Kurokawa Lab (Li et al.)	25	5	iCell	30		2							5
ICaL	Es-Salah-Lamoureux et al.	room	15-17	IHC			5					5	2	
	Veerman et al.	36	21	IHC			1.8							
	Ma et al. (2011)	room	5	iCell			5					5	2	
ICaT	Kurokawa Lab	36	2	iCell			5							5
Ikr	Bellin et al.	37	14	IHC	140	5	1.8		20	125				
	Es-Salah-Lamoureux et al.	35	21	IHC	140	4	1		20	125				
	Ma et al. (2011)	35-37	8	iCell	150	5	1.8		##			5	2	
	Wu Lab (Garg et al.)	36-37	4	IHC	150	5	1.8		##					
Ito	Veerman et al.	36	13	IHC	140	5	1.8		20	105		5		
	Cordeiro et al.	36	14	iCell	126	5	2		10		125	10	5	
	Ma et al. (2011)	35-37	8	iCell		5		160		150			5	
Iks	Ma, Wei et al. (2015)	37	7/8	IHC/iCell	140	5	1.7		50		80			
	Ma et al. (2011)	35-37	5	iCell	150	5	1.8		20		125			
If	Kurokawa Lab (Li et al.)	36	9	iCell	135	5.4	1.8		30				1	
	Ma et al. (2011)	35-37	17	iCell	135	5.4	1.8		150			5	2	
IK1	Ma et al. (2011)	35-37	4	iCell		5.4		160		150				
	Herron et al. (PDMS/ glass)	21-22	5/7	iCell	148	5.4	1.8		148					
	Kurokawa Lab (Li et al.)	36	7	iCell	135	5.4	1.8		20				1	

*IHC = in-house control cell-line

Table 2:

Reference:	**Cell-Line**	**n =**	**Cell-type**
Wu Lab (A)	IHC	14	Ventricular-like
Wu Lab (B)	IHC	12	
Herron et al. (PDMS- Mature)	iCell	24	Mixed Morphologies
Herron et al. (Glass- Immature)	iCell	37	
Ma et al. (2011)	iCell	32	Ventricular-like
Doss et al. (Group A)	iCell	63	Ventricular-like
Doss et al. (Group B)	iCell	23	
Cordeiro et al.	iCell	149	Mixed Morphologies
Es-Salah-Lamoureux et al.	IHC	9	Ventricular-like
Ma, Wei et al. (2015)	IHC	17	Ventricular-like

*IHC = in-house control cell-line

Table 3:

Parameter	*Value*	*Units*	*Definition*
k_{NCX}	1100	pA/pF	Maximal I_{NCX}
γ	0.7	-	Voltage-dependence parameter (I_{NCX})
K_{mCa}	1.38	mM	Ca_i half-saturation parameter (I_{NCX})
K_{mNa}	87.5	mM	Na_i half-saturation parameter (I_{NCX})
k_{sat}	0.1	-	Saturation Factor (I_{NCX})
α	2.75	-	Outward enhancing factor (I_{NCX})
P_{NaK}	2.48	pA/pF	Maximal I_{NaK}
K_{mK}	1.0	mM	K_o half-saturation parameter (I_{NaK})
K_{mNa}	40.0	mM	Na_i half-saturation parameter (I_{NaK})
g_{PMCA}	0.2625	nS/pF	Maximal I_{PMCA} Conductance
K_{PMCA}	0.0005	mM	Ca_i half-saturation parameter (I_{PMCA})
k_s	12.5	ms^{-1}	SR release rate constant (I_{Rel})
k_{oCa}	643750	$mM^{-2}ms^{-1}$	Non-SR-dependent transition rate constant (J_{Rel})
k_{om}	0.2143	ms^{-1}	J_{Rel} Rate Constant
k_{iCa}	18.495	$mM^{-1}ms^{-1}$	Non-SR-dependent transition rate constant (J_{Rel})
k_{im}	0.00056	ms^{-1}	J_{Rel} Rate Constant
$EC_{50\text{-}SR}$	0.45	-	Parameters for $[Ca]_{SR}$-dependent activation of SR release (J_{Rel})
Max_{SR}	15	-	
Min_{SR}	1	-	
k_{CaSR}	$Max_{SR} - \frac{(Max_{SR} - Min_{SR})}{1 + \left(\frac{EC_{50-SR}}{[Ca]_{SR}}\right)^{2.5}}$		$[Ca]_{SR}$- dependent RyR activation coefficient (J_{Rel})
k_{oSRCa}	$\frac{k_{oCa}}{k_{CaSR}}$		J_{Rel} Rate Constant

k_{iSRCa}	$k_{iCa} * k_{CaSR}$		J_{Rel} Rate Constant
$V_{max,up}$	1.105e-4	mM/ms	Maximal J_{up}
K_{up}	1.755e-4	mM	Half-saturation constant
V_{leak}	1.6e-6	ms^{-1}	Maximal J_{leak}

Table 4:

	TTX	Nifedipine	E-4031
Concentration	10 μM	30nM	10nM
Ionic Current Blocked	I_{Na}	I_{CaL}	I_{Kr}
Range of IC50s (nM)	640-1355[1,2]	30-39[1,3,4]	7-17[3,4,5]
% Current Block	88-94%	72-77%	47-59%
Output Measured	Max Upstroke Velocity	APD_{90}	APD_{90}
Experimental Output w/ Drug (range of dataset means)	16.7-60%[1,6,7]	67.7-88.9%[1,3,4,8]	113-160%[1,3,4,8]
Output w/ Drug in Model Subpopulation	48.6 ± 27.5%	89.8 ± 5.1%	121.8 ± 10.4%
Model Subpopulation n=	1057	11894	8398

(1) Ma et al., 2011 (2) Moreau et al., 2017 (3) Peng et al., 2010 (4) Gibson et al., 2014 (5) Harris et al., 2013 (6) Scheel et al., 2014 (7) Jonsson et al., 2012 (8) Hortigon-Vinagre et al., 2016

First Author Profile:

Divya Kernik is currently a PhD candidate in Biomedical Engineering at the University of California, Davis. She obtained a BS in Biomedical Engineering from Johns Hopkins University. The focus of her PhD work has been in developing computational methods to understand human-derived cardiac cells, as presented here. In the future, she aims to continue to use computational modeling to address questions in cardiac physiology and pharmacology, with the underlying goal of incorporating human diversity throughout these efforts.

FIGURE LEGENDS:

Figure 1: A schematic of the computational iPSC-CM model. Red stars indicate individual currents (*I_{Na}, I_{CaL}, I_{Kr}, I_{Ks}, I_{K1}, I_{to}, and I_f), formulated using single-exponential voltage-dependent rate constants. Parameters were optimized to experimental iPSC-CM kinetic data. The mathematical formulation for an example current, I_{Na}, is shown in the right panel. All gating variables in the starred currents were modeled using the example formula for gating variable x. Additional calcium-dependent currents (I_{NCX}, I_{PMCA}, I_{CaT}, and SR currents: I_{SERCA}, I_{RyR}, and I_{leak}) were modeled using previously published model formulations, optimized to calcium transient data from iPSC-CMs. Remaining currents (I_{NaK}, I_{bCa}, I_{bNa}) were modeled using ten Tusscher 2004 formulations optimized to recapitulate iPSC-CM AP data.

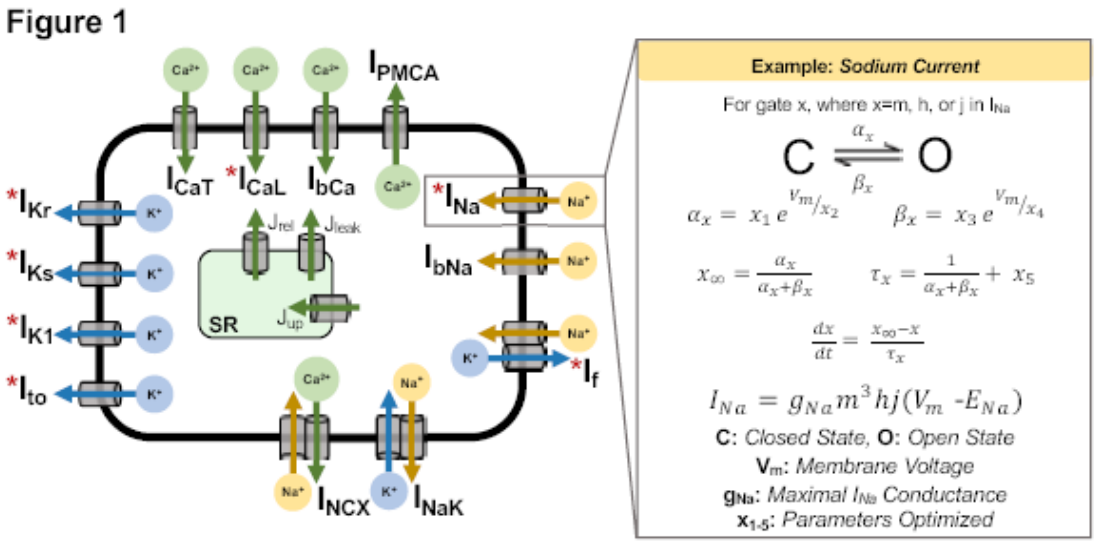

Figure 2: A flow chart showing the methodology for building the iPSC-CM model populations.

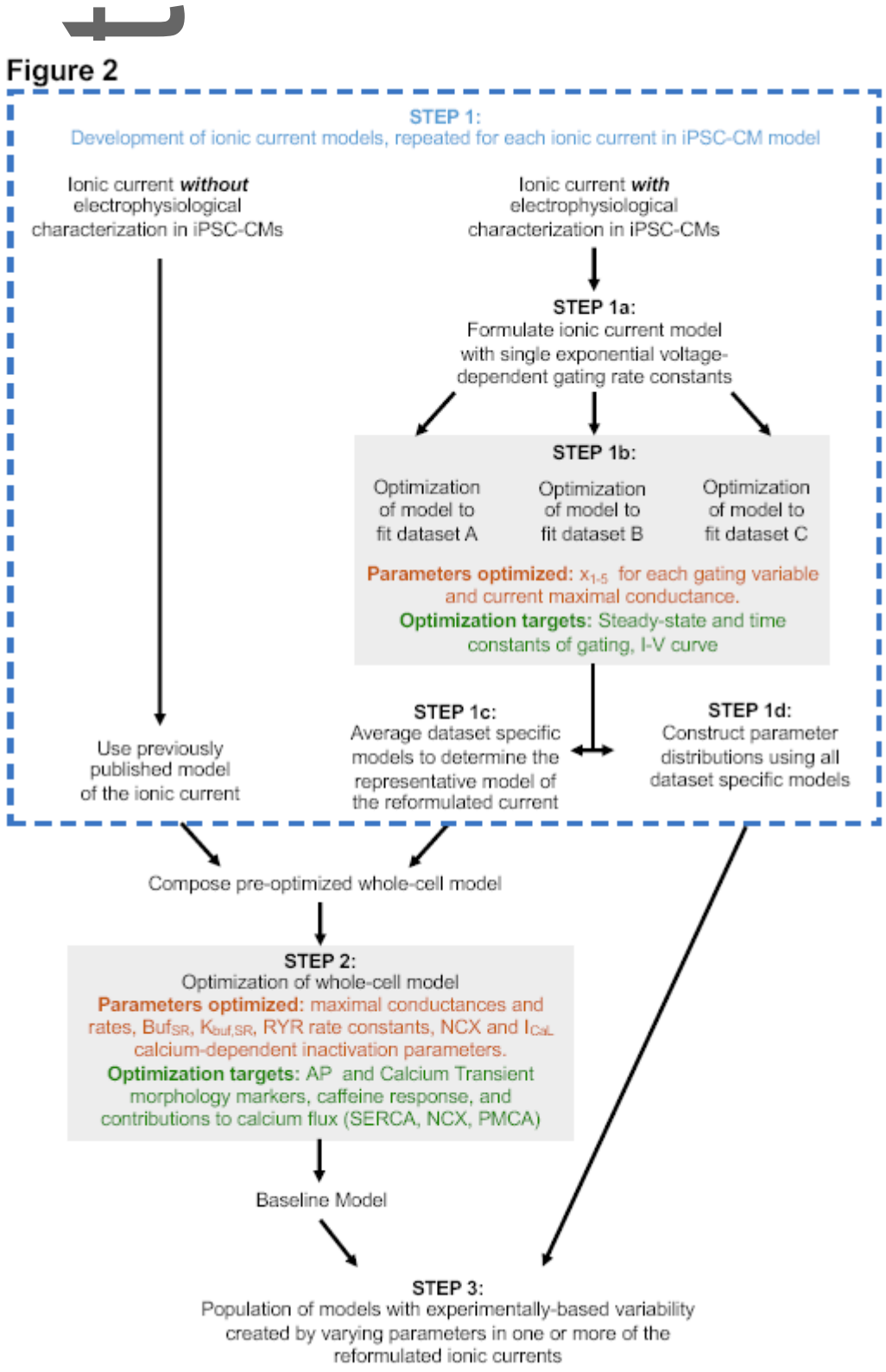

Figure 3: Sodium current (I_{Na}) model optimization. **(A)** Steady state inactivation and activation curves. Dataset-specific model fits (lines) optimized to experimental data (points). The sodium current model used in the baseline whole-cell model is shown in black. Colors represent distinct experimental iPSC-CM data from Ma et al. (Ma *et al.*, 2011), and from immature and mature cell preparations from the Jalife lab (published in Herron et al. (Herron *et al.*, 2016)). **(B)** I-V curves for I_{Na}. Dataset-specific models were simulated using the experimental conditions of the corresponding experimental data. **(C)** I_{Na} activation (m-gate) time constants. **(D)** I_{Na} fast-inactivation (h-gate) time constants. **(E)** I_{Na} slow-inactivation (j-gate) time constants. J-gate time constant parameters for all I_{Na} models were optimized to experimental iPSC-CM data from the Kurokawa lab.

Figure 3

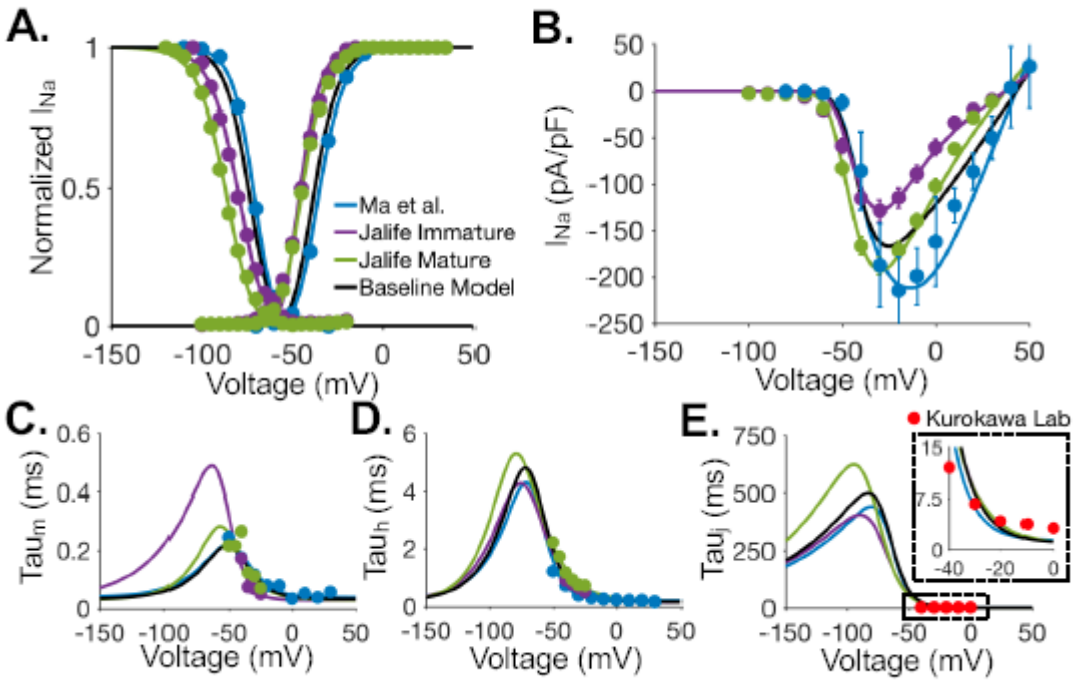

Figure 4: Calcium current model optimization. **(A)** L-type calcium current (I_{CaL}) steady state inactivation and activation curves with dataset-specific model fits (lines) optimized to experimental data (points). The L-type calcium model used in the baseline cellular model is shown in black. Colored symbols represent experimental iPSC-CM data from Ma et al.(Ma *et al.*, 2011), Veerman et al. (Veerman *et al.*, 2016), and Es-Salah-Lamoureux et al. (Es-Salah-Lamoureux *et al.*, 2016). **(B)** I-V curves for I_{CaL}. Calcium-dependent gating model formulation retained from ten Tusscher 2004 adult cardiomyocyte model with parameter optimization to fit whole cell iPSC-CM outputs. **(C)** Time constants of I_{CaL} activation gate. Time constant parameters for all I_{CaL} models were optimized to experimental iPSC-CM data from Ma et al. (Ma *et al.*, 2011). **(D)** Time constants of I_{CaL} inactivation gate. **(E)** Optimization of peak T-type calcium current (I_{CaT}) to experimental iPSC-CM data from the Kurokawa lab. Model formulation of I_{CaT} was retained from the Maltsev and Lakatta sinoatrial node model.

Figure 4

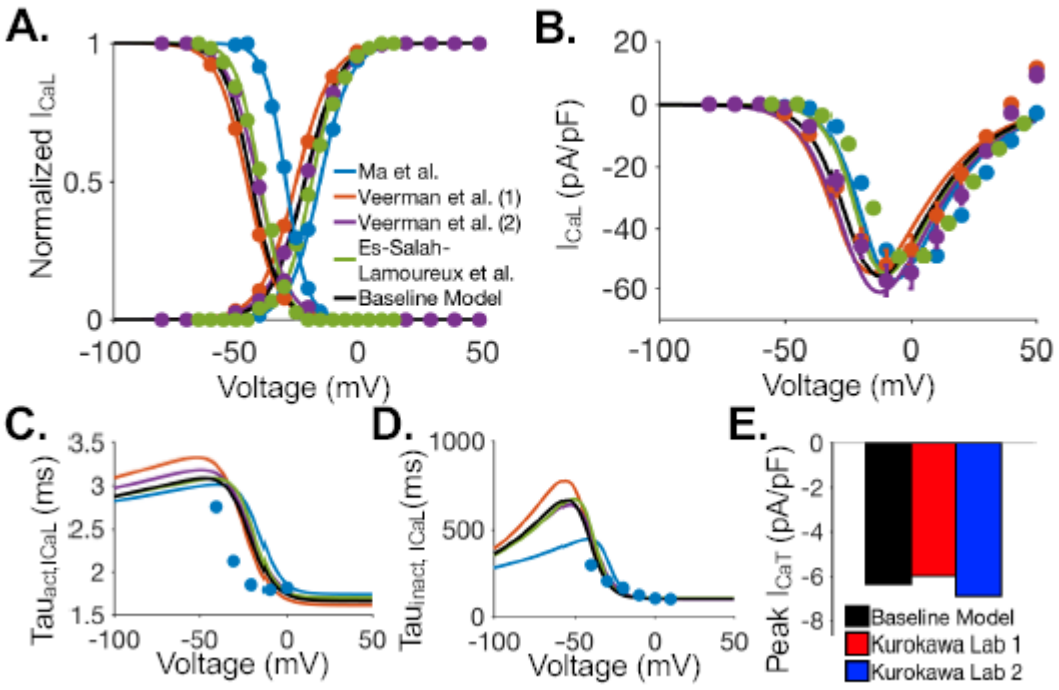

Figure 5: Rapid delayed rectifier potassium current (I_{Kr}) model optimization. **(A)** Steady state activation with dataset-specific model fits (lines) optimized to experimental data (points). The I_{Kr} model used in the baseline cellular model is shown in black. Colored symbols represent experimental iPSC-CM data from Ma et al. (Ma *et al.*, 2011), the Wu lab, Es-Salah-Lamoureux et al. (Es-Salah-Lamoureux *et al.*, 2016) ,and Bellin et al. (Bellin *et al.*, 2013). For I_{Kr} inactivation gating, existing ten Tusscher 2004 model components were reformulated to single exponential forms. **(B)** I-V curves for I_{Kr}. **(C)** Time constants of I_{Kr} activation gate. Activation time constants for the Ma et al., Wu lab, and Es-Salah-Lamoureux et al. models were optimized to experimental iPSC-CM data from Ma et al. (Ma *et al.*, 2011). **(D)** Time constants of I_{Kr} inactivation gate using the ten Tusscher 2004 model reformulated to single exponential forms.

Figure 5

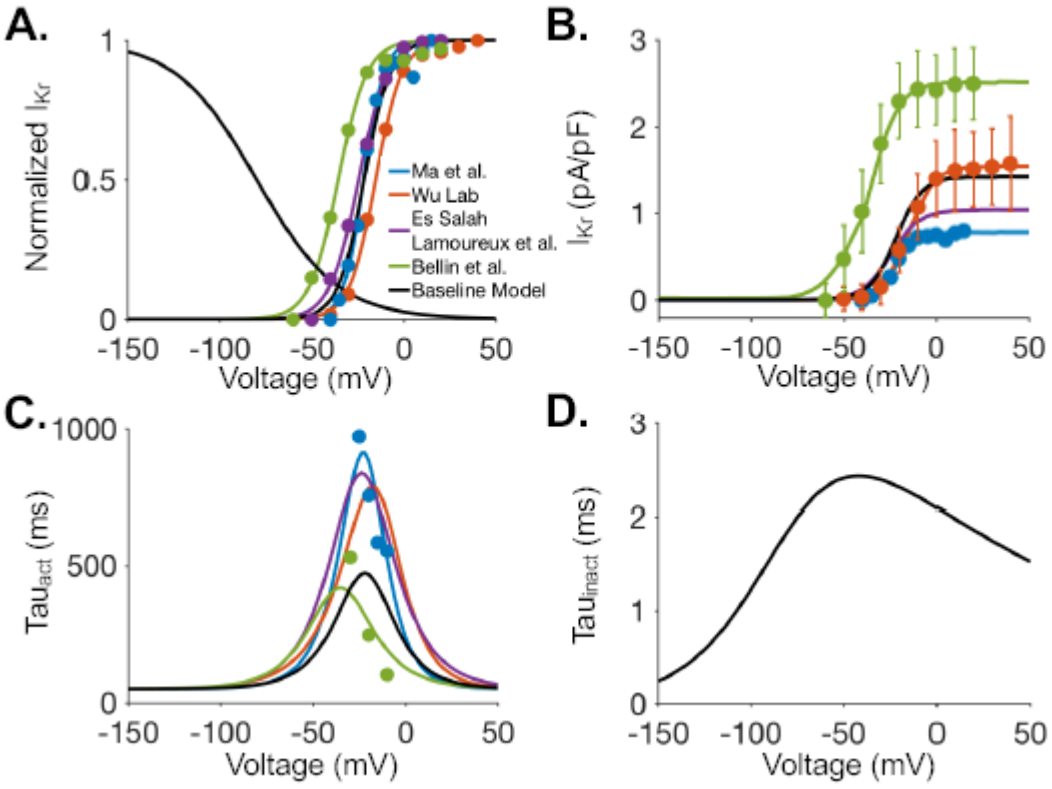

Figure 6: Transient outward potassium current (I_{to}) model optimization. **(A)** Steady state activation and inactivation curves with dataset-specific model fits (lines) optimized to experimental data (points). The I_{to} model used in the baseline cellular model is shown in black. Colored symbols represent experimental iPSC-CM data from Veerman et al. (Veerman *et al.*, 2016), Ma et al. (Ma *et al.*, 2011), and Cordeiro et al. (Cordeiro *et al.*, 2013). **(B)** I-V curves for I_{to}. **(C)** Time constants of I_{to} activation gate. For activation time constants in all I_{to} models, the ten Tusscher 2004 I_{to} activation time constants were reformulated to single exponential forms. **(D)** Time constants of I_{to} inactivation gate. Veerman et al. model time constant parameters were optimized to iPSC-CM experimental data from Ma et al. (Ma *et al.*, 2011).

Figure 6

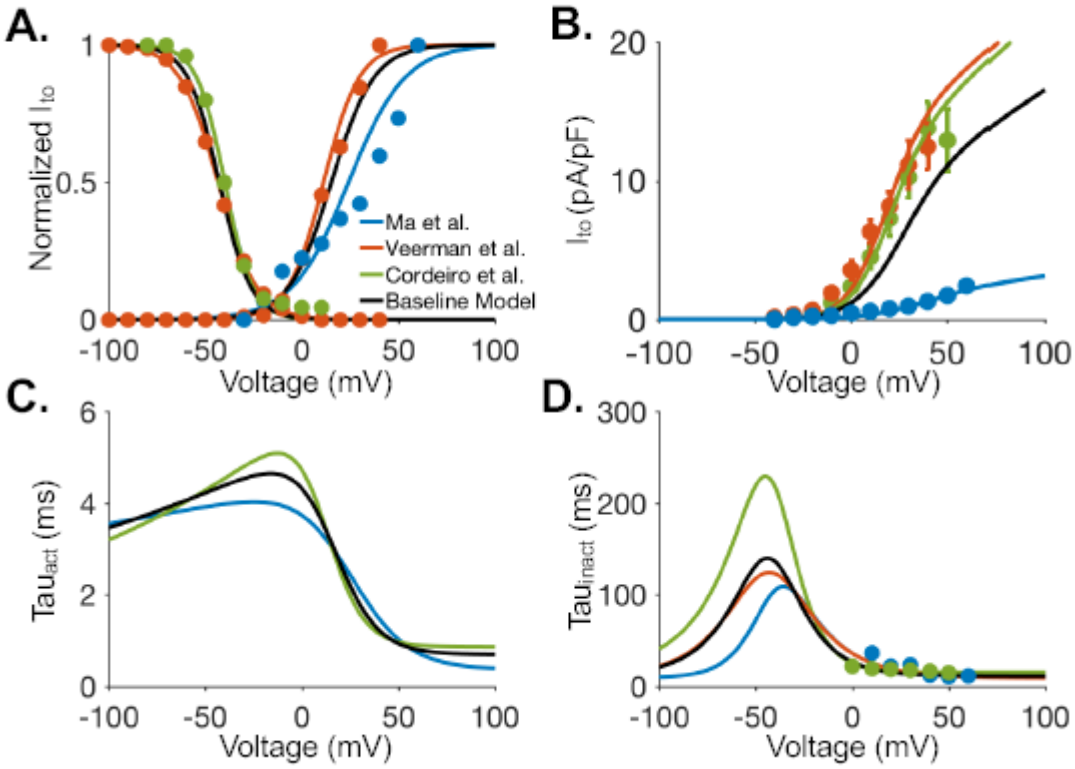

Figure 7: Slow delayed rectifier potassium current (I_{Ks}) model optimization. **(A)** Steady state activation with dataset-specific model fits (lines) optimized to experimental data (points). The I_{Ks} model used in the baseline cellular model is shown in black. Colored symbols represent experimental iPSC-CM data from Ma et al. (Ma *et al.*, 2011), and two separate iPSC-CM cell-line datasets in Ma, Wei et al. (Ma *et al.*, 2015). **(B)** Time constants of I_{Ks} activation gate. Time constants for all I_{Ks} models were optimized to experimental iPSC-CM data from Ma et al. (Ma *et al.*, 2011). **(C)** I-V curves for I_{Ks}.

Figure 7

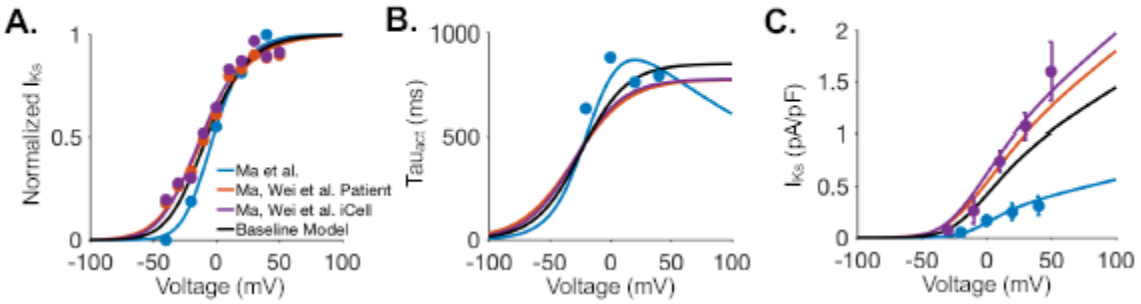

Figure 8: Pacemaker/funny current (I_f) model optimization. **(A)** Steady state activation with dataset-specific model fits (lines) optimized to experimental data (points). The I_f model used in the baseline cellular model is shown in black. Colored symbols represent experimental iPSC-CM data from the Kurokawa lab and Ma et al. (Ma *et al.*, 2011). **(B)** Time constants of I_f inactivation gate. **(C)** I-V curves for I_f.

Figure 8

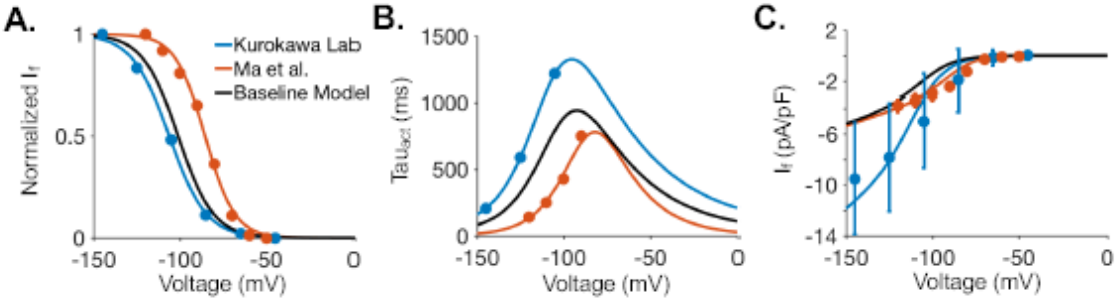

Figure 9: Inward rectifier potassium current (I_{K1}) model optimization. I-V curves for I_{K1} with dataset-specific model fits (lines) optimized to experimental data (points). The I_{K1} model used in baseline cellular model is shown in black. Colored symbols represent experimental iPSC-CM data from Ma et al. (Ma *et al.*, 2011), the Kurokawa lab, and immature and mature cell preparations from the Jalife lab (published in Herron et al. (Herron *et al.*, 2016)).

Figure 9

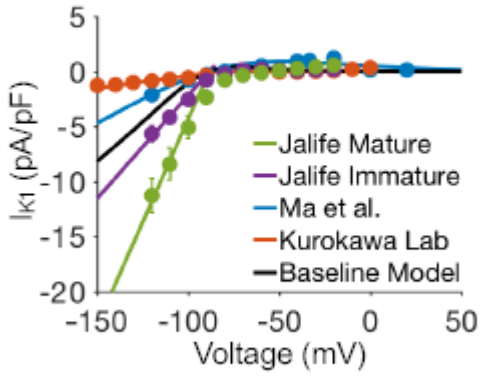

Figure 10: Optimization of calcium handling in the iPSC-CM baseline model. **(A)** Experimental iPSC-CM calcium transient (CaT) traces from the Wu lab (grey) with baseline model CaT (red). Experimental data was reported as normalized Ca^{2+} florescence (F_{ratio}). Separately, average iPSC-CM peak and diastolic Ca^{2+} concentrations were measured by the Wu lab. The two y-axes are plotted so the average F_{ratio} peak and diastolic values of the experimental dataset shown correspond to the average experimental concentration of peak and diastolic Ca^{2+} (in panel B). The baseline model CaT output is in nM. **(B)** Comparison of baseline model CaT morphology markers to experimental iPSC-CM data from the Wu lab. **(C)** Relative contribution of calcium from I_{SERCA}, I_{NCX}, and I_{PMCA} to the CaT during a single AP in the baseline model. **(D)** Comparison of experimental (black and white) and baseline model (colored) relative contribution of calcium flux from I_{SERCA}, I_{NCX}, and I_{PMCA} during the CaT. Experimental data from Hwang et al. (Hwang *et al.*, 2015).

Figure 10

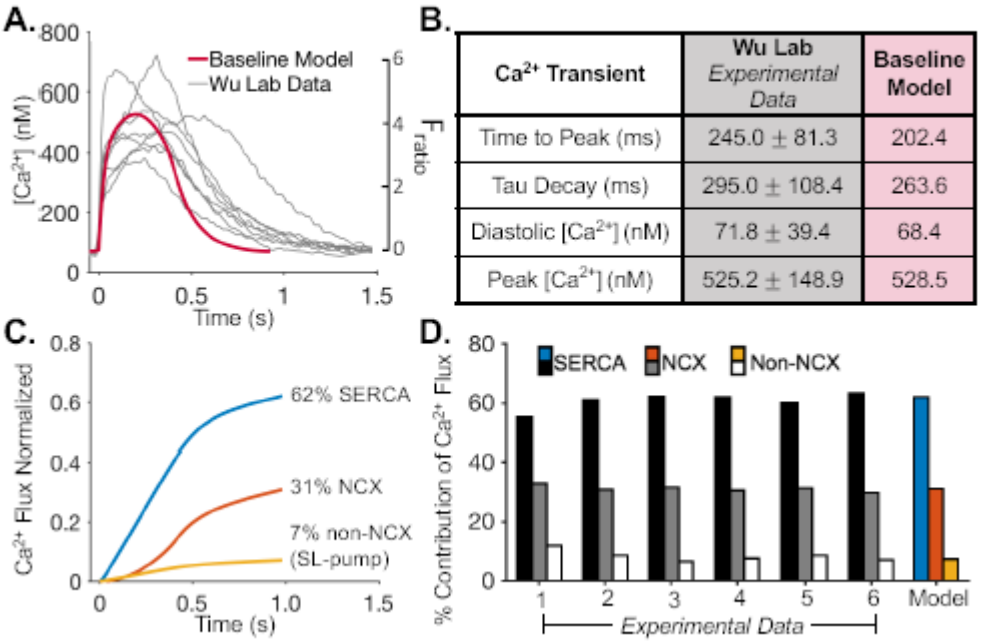

Ca^{2+} Transient	Wu Lab *Experimental Data*	Baseline Model
Time to Peak (ms)	245.0 ± 81.3	202.4
Tau Decay (ms)	295.0 ± 108.4	263.6
Diastolic $[Ca^{2+}]$ (nM)	71.8 ± 39.4	68.4
Peak $[Ca^{2+}]$ (nM)	525.2 ± 148.9	528.5

Figure 11: Characterization of the baseline model action potential (AP). **(A)** Time course of the spontaneously beating APs in the baseline model. **(B-D)** Comparison of AP morphology in the baseline model (red) and experimental iPSC-CM data (black). Experimental data from the Wu Lab, the Jalife Lab, Ma et al. (Ma *et al.*, 2011), Doss et al. (Doss *et al.*, 2012), Cordeiro et al. (Cordeiro *et al.*, 2013), Es-Salah-Lamoureux et al. (Es-Salah-Lamoureux *et al.*, 2016), and Ma et al. (Ma *et al.*, 2015). **(E)** Sensitivity analysis using multivariable regression in the baseline model. Only parameters with regression coefficients > 0.3 shown.

Figure 11

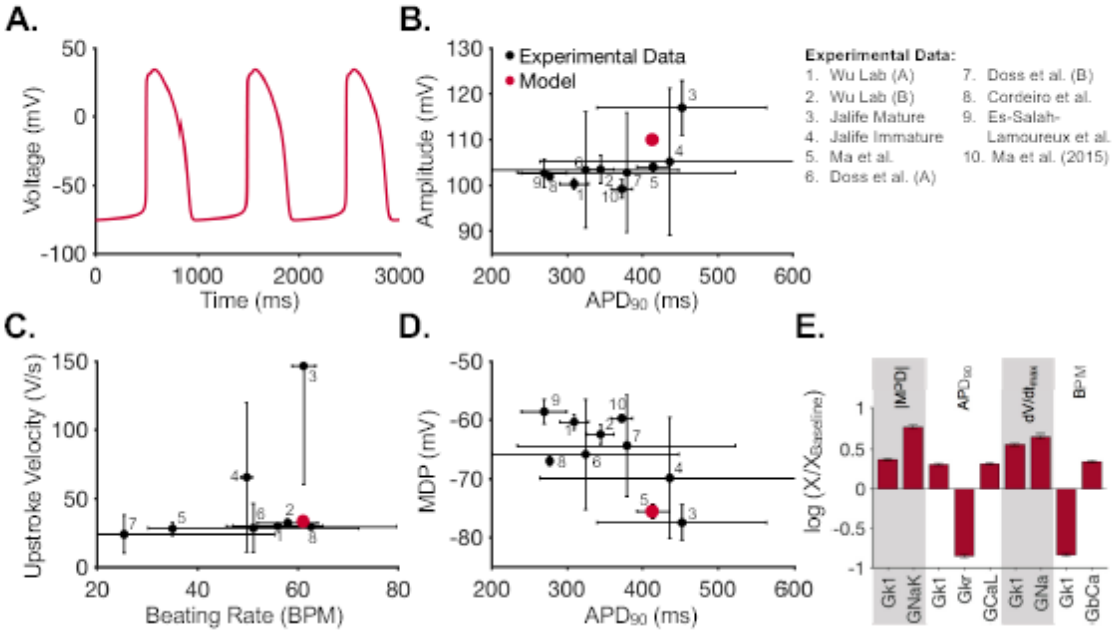

Figure 12: Kinetic variability generated by varying individual current model parameters. Steady-state and time constant curves for each gate in **(A)** I_{Na}, **(B)** I_{CaL}, **(C)** I_{Kr}, and **(D)** I_F. **(E)** IV curves for I_{K1}. All panels include: dataset-specific model fits (black lines, also shown in Fig. 3-10), randomly-parameterized models resulting in spontaneous AP generation in the cell models (colored lines), and randomly-parameterized models resulting in non-spontaneous or non-AP generating model cells (grey lines).

Figure 12

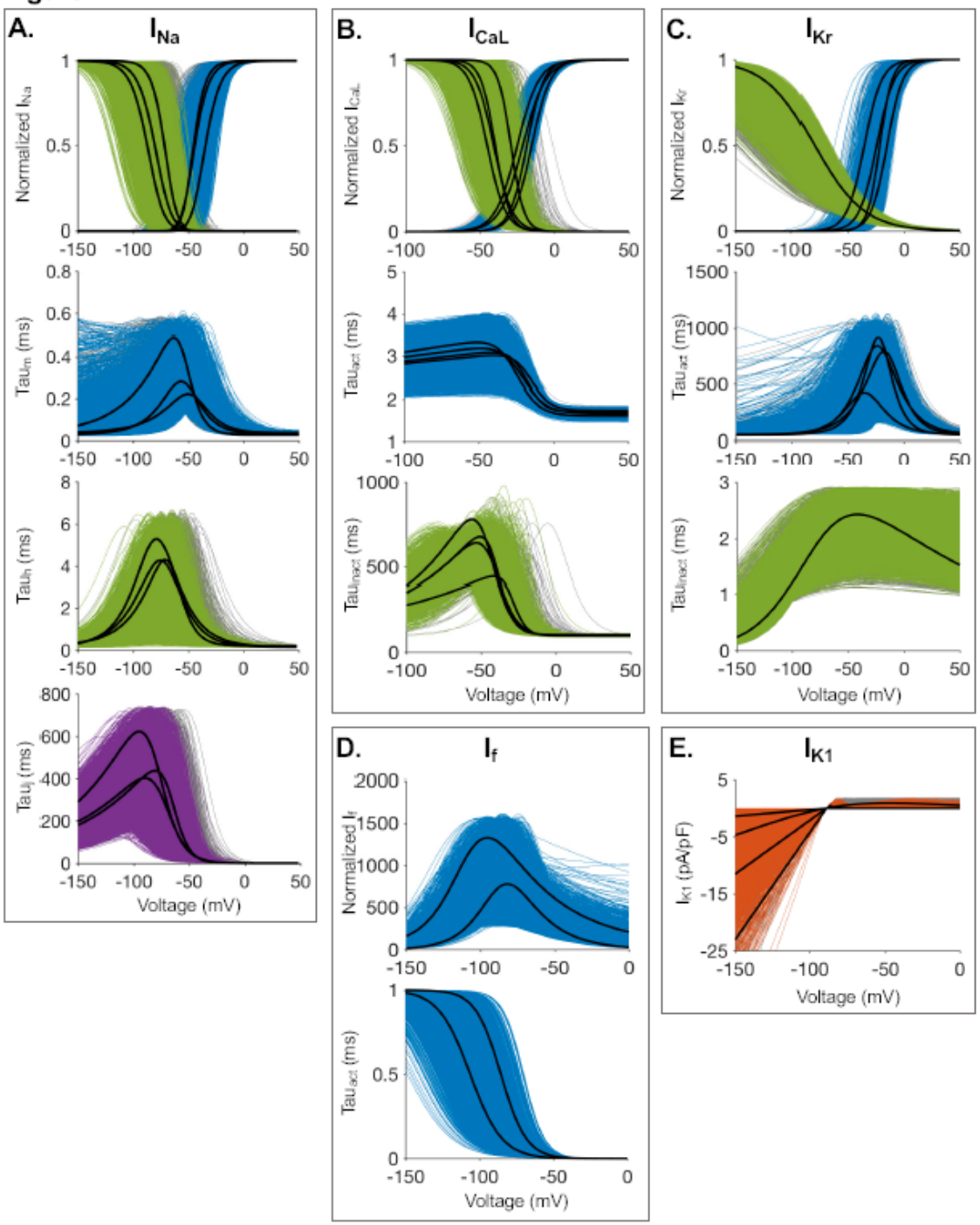

Figure 13: **(A**) APs of spontaneously beating cells (n=25434) generated by varying one current at a time (I_{Na}, I_{CaL}, I_{Kr}, I_F, and I_{K1}). **(B)** APs of spontaneously beating cells (n=17139) generated by varying the same five currents simultaneously. **(C)** Representative AP time courses of spontaneously beating cells at various pacing frequencies. **(D-F)** Comparison of AP morphology in the populations of models (color) and experimental iPSC-CM data (black). Each colored point represents a spontaneously beating cell created by varying a single current (as shown in A), or by varying all five currents simultaneously (as shown in B). **(G)** Mean and standard deviations of AP morphology measures for each population, normalized to the baseline model AP.

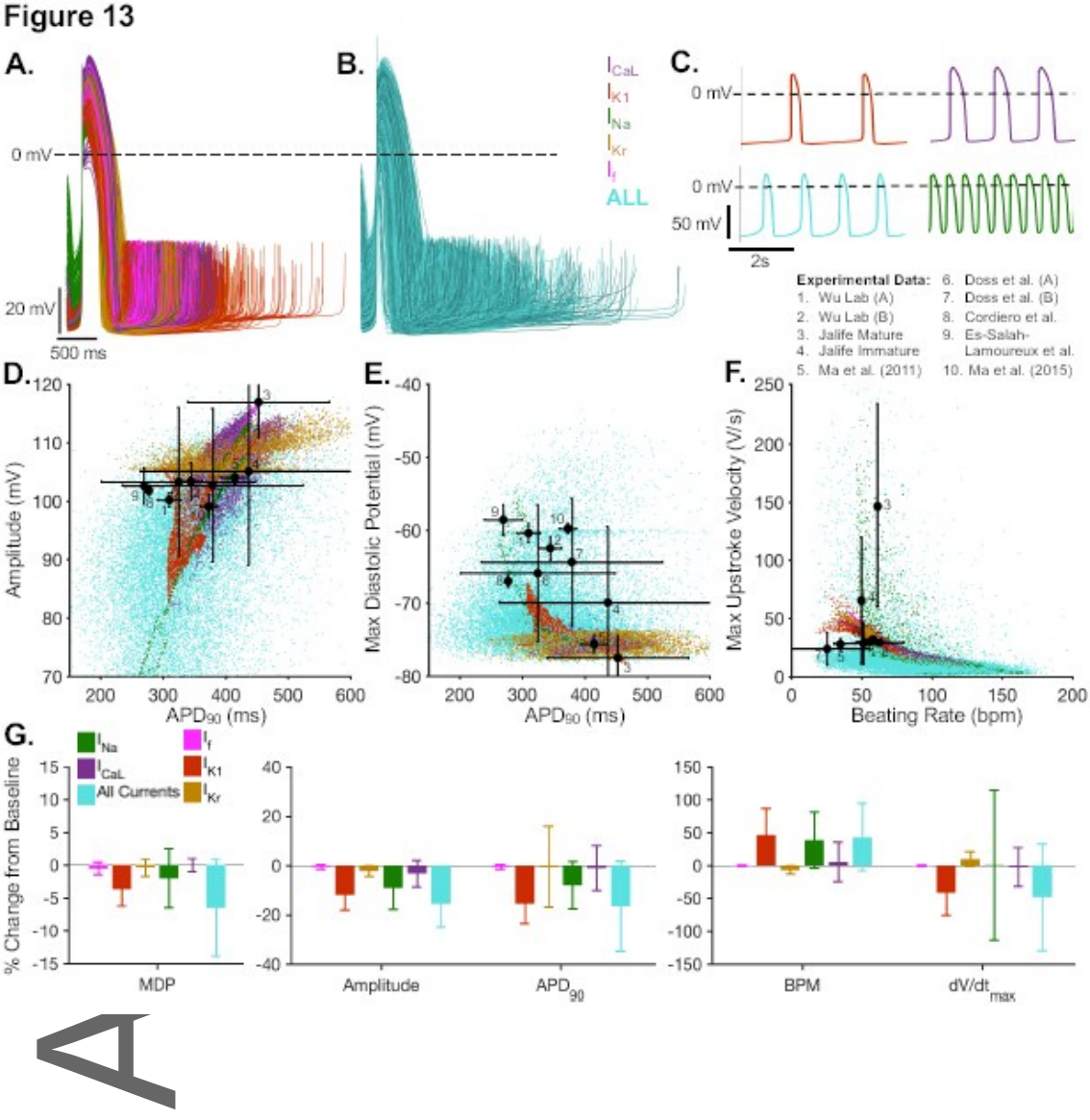

Figure 14: Sample APs showing the effect of ion channel blockers within the model population. Each panel shows the same cellular models in the control (solid lines) and drugged (dashed lines) conditions. Three cells are shown for each drug, representing a cell with a change in the given AP parameter near the population mean (cell 2), and +/- one standard deviation. The mean and standard deviations for the full population are described in Table 4. Drug effects are shown for **(A)** Tetrodotoxin (TTX) **(B)** Nifedipine **(C)** E-4031.

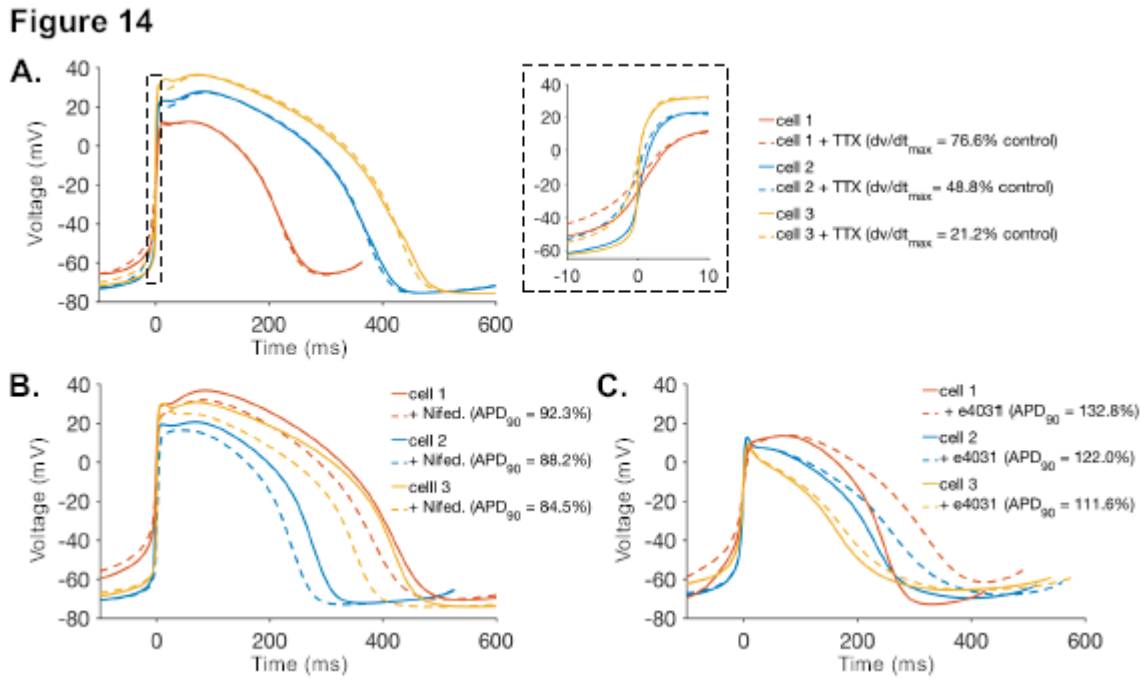

Figure 15: Comparison of immature and mature cellular models. **(A)** AP for the immature (baseline) cellular model, compared to AP for a representative mature cellular model. Immature and mature cellular models determined by scaling G_{K1} and G_{Na} based on peak currents reported in iPSC-CMs with control (immature) and maturation-promoting cell preparations (Herron et al.). **(B)** Comparison of models and experimental AP morphology for mature and immature cell-types. Experimental data shown from the Jalife Lab, as published in Herron et al. (Herron *et al.*, 2016). All model and experimental data was normalized to the Jalife Lab mature experimental dataset average. **(C)** Comparison of sensitivity analysis immature and mature models using multivariable regression. Only parameters with regression coefficients > 0.3 shown.

Figure 15

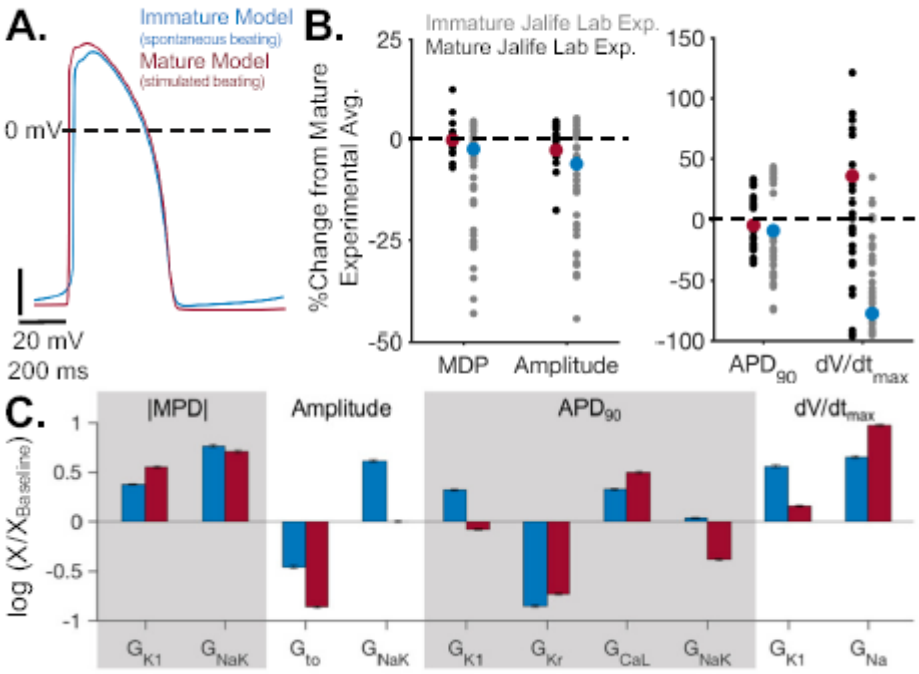

Figure 16: Comparison of mature and immature iPSC-CM model subpopulations. **(A)** Division of model population into mature and immature phenotypes (using five-current variation population with simultaneous variation in I_{Na}, I_{CaL}, I_{Kr}, I_F, and I_{K1} parameters). Experimental data shown from the Jalife Lab, as published in Herron et al. Model subpopulation shown in red (n=325) represents mature phenotypes with MDP below -75mV and maximal upstroke velocity greater than 85 V/s. Model subpopulation shown in blue (n=13759) represents immature phenotypes with MDP above -75mV and maximal upstroke velocity below 85 V/s. Model subpopulation shown in grey was not analyzed in this comparison. **(B)** The four model parameters with the largest difference between the mature and immature model subpopulations. For each subpopulation, parameter averages and standard deviations are shown as percent change from the baseline model parameter value. **(C)** Steady-state inactivation for I_{Na} in the mature and immature model subpopulations. Individual cells (light colors) and subpopulation average parameter values (darker colored lines) are shown. **(D)** Peak I_{K1} and I_{Na} for the I-V relationship of each cell in the model subpopulations was compared to data reported in Herron et al. (Herron *et al.*, 2016). Model and experimental values are shown as the percent change from the immature to mature phenotype.

Figure 16